

Utrecht University

Faculty of Science

***t*-butyl-Terrylene:
novel singlet fission material for
highly efficient solar cells**

Maria Antonietta Mione

Student No.: 4204492

Hybrid Solar Cells group

Thesis supervisors:

Dr. Bruno Ehrler

Prof. Dr. Kobus Kuipers

Second supervisor:

Dr. Dries van Oosten



Universiteit Utrecht

Abstract

Singlet fission is a process occurring in some organic semiconductors which allows for extracting two charges per incoming photons. Solar cells employing a singlet fission material coupled with a low bandgap material have the potential to exceed the Shockley-Queisser limit by exploiting enhanced photocurrent from high energy photons in addition photocurrent from low energy photons. Here, we fabricated singlet fission solar cells in both a one- and a two-bandgap structure with a stable, newly synthesized singlet fission material, 2,5,10,13-tetra(tert-utyl)terrylene (*t*-butyl-Tr). Both architectures showed promising performances. The one-bandgap device, fabricated in a bilinear *t*-butyl-Tr/C₆₀ heterojunction architecture showed $J_{SC} = 2.6 \text{ mA/cm}^2$, $V_{OC} = 0.49 \text{ eV}$ and PCE=0.37%. The two-bandgap inverted PbS QDs/*t*-butyl-Tr architecture showed enhanced open circuit voltage $V_{OC} = 0.57 \text{ eV}$, PCE=0.52% with a photocurrent contribution from both QDs and *t*-butyl-Tr.

Acknowledgements

My first and biggest thanks goes to my supervisor Bruno Ehrler who gave me the unique possibility to perform valuable research in such an inspiring, sparkly place as AMOLF. I could not have had better supervision and guidance than what Bruno provided me through this year I spent focusing on this totally new field. I can honestly say it was my true pleasure to ship the Hybrid Solar Cells Lab and see it becoming crowded and crowded. A special thanks to the all group, to all the occasional guests I saw coming and going and to those people I had the luck to know for few months or weeks. In particular, thanks to Jumin Lee, TianYi Wang and Le Yang for their scientific and moral support. Still, life in the lab would not have been as easy as it was without the technical support of Marc Duursma. Finally, I would also acknowledge Erik Garnett, Nanoscale Solar Cells group, for making his equipment available for me and, of course, the PhD students Sander Mann, Parisa Khoram and Sarah Brittman who kindly helped with some important measurements.

Table of contents

Introduction

1 Background

1.1 Semiconductor materials: energy band and electrical conductivity.....	2
1.2 Working principle of a solar cell.....	2
1.2.1 Solar cell parameters.....	3
1.2.2 Solar spectrum and air mass.....	5
1.2.3 Shockley-Queisser limit.....	5
1.3 Organic semiconductors.....	7
1.3.1 Band structure and conductivity.....	7
1.4 Organic solar cells.....	8
1.4.1 OPV device structures.....	9
1.5 Singlet fission.....	10
1.5.1 Singlet fission in photovoltaics.....	12
1.5.2 Singlet fission materials.....	13
1.6 Motivation.....	14

2 Experimental methods

2.1 One-bandgap device fabrication.....	18
2.2 Two-bandgap device fabrication.....	18
2.3 Deposition techniques.....	21
2.4 Characterization techniques.....	21

3 Results

3.1 One-bandgap device with P3HT as triplet blocking layer.....	25
3.2 One-bandgap device without P3HT as triplet blocking layer.....	29
3.3 Two-bandgap device.....	30

Conclusions and outlook.....	34
------------------------------	----

Bibliography.....	36
-------------------	----

Introduction

Throughout history we observe a close correlation between socio-economic development and the demand for energy, from wood to coal and nowadays oil. With a constantly increasing world population it is wise and necessary to search for clean, alternative sources of energy to replace, at least partially, non-renewable fossil fuels which today is the dominating source of electric energy.

Forms of renewable energy rely on the sun, wind or water. The sun is the most powerful source of clean, nearly unlimited energy and the conversion of solar energy into electricity is probably one of the most exciting research challenges nowadays. Since the physical phenomenon responsible for converting light to electricity - the photovoltaic effect - was first observed in 1879 [1], solar energy physics has known an ever-increasing interest intended to realize more and more efficient devices. Unfortunately, photovoltaic conversion is limited due to the broad spectrum of incoming sunlight. This limitation is known as Shockley-Queisser limit which sets the maximum efficiency for silicon solar cells at 34% [2]. Besides, part of the scientific and commercial concern is focused on lowering manufacturing costs by engineering non expensive material and developing cheap fabrication techniques.

Singlet fission, a process able to convert one photon into two electric charges, has received particular attention over the past decade as a powerful tool to overcome the Shockley-Queisser limit. In fact, it has been shown that by combining a single fission material with a low bandgap material the maximum efficiency limit can be brought to 44% by making better use of the solar spectrum [3]

]. In such a system high energy photons would create enhanced photocurrent in the singlet fission material, while the low energy photons would produce direct photocurrent in the low bandgap material. Further, singlet fission is a process occurring in organic semiconductors which are well known for their high chemical and physical tuneability, ease of processing and low cost manufacturing.

However, common singlet fission materials are unstable in light and air and for this reason not always suitable for photovoltaic application. In this project a newly synthesized terrylene-based singlet fission material is used for solar cell fabrication. Higher photostability and favorable energy levels that match the bandgap of silicon render it a promising candidate for application in photovoltaics.

The first chapter introduces general concepts with particular focus on the working principle of a solar cell, the physics of the singlet fission process and its use in photovoltaic technology.

The second chapter describes experimental methods and techniques used for solar cell fabrication and characterization, for two different device architectures.

In the third chapter results for both architectures will be presented and discussed.

Chapter 1

Background

In this chapter the main theoretical basis of the project is reported. Firstly, the physics of semiconductors and working principle of a solar cell are briefly explained. Then, a picture of organic solar cells and how they differ from inorganic ones is given. Finally, singlet fission process will be introduced with particular focus on how this process could be used to overcome the Shockley-Queisser efficiency limit for single junction solar cells.

1.1 Semiconductor materials: energy bands and electrical conductivity

In a solitary atom, electrons around the nucleus occupy discrete energy levels but in the case of atoms in a crystal this discrete energy distribution is replaced by the energy band structure. This is due to the interaction between atoms, whereas dimension and separation of the bands depend on the characteristic distance between nuclei inside the crystal. In solid-state physics the electronic band structure describes which range of energy an electron inside the solid can have and which energies are forbidden for it. Semiconductors are materials with forbidden energy band called bandgap between two allowed bands: the valence band at lower energy and the conduction band at higher energy.

At absolute zero temperature electrons occupy the lowest energy levels respecting Pauli's principle. The highest occupied energy level is the Fermi level which is important in order to define the conductivity of materials. For semiconductors, the Fermi level lies within the bandgap. As the temperature increases, electrons start to fill higher energy levels and for every temperature T the probability to find an electron at energy levels higher than the Fermi level is given by the Fermi-Dirac statistic

$$f(E) = \frac{1}{e^{(E-E_F)/kT} + 1} \quad (1.1)$$

where E_F is the Fermi energy and k is the Boltzmann constant [4].

By introducing the Fermi-Dirac statistic we can describe the differences between metals, semiconductors and insulators. Generally, electrons inside a band can contribute to the electrical conductivity only if the band is partially filled so that there will be free energy levels where electrons can transfer once an external electromagnetic field is applied. As a result the distribution of electrons in the allowed band determines the behaviour of the material. Metals present part of the valence band filled with electrons so that the Fermi energy level lies in the band. In insulators and semiconductors, electrons fill the entire band and the Fermi level is inside a band gap; however, in semiconductors the bands are close enough to the Fermi level to be thermally populated.

High conductivity in a material originates from many partially filled states and high level of delocalization. At low temperatures a semiconductor is not conductive. As temperature increases, sufficient energy is transferred to a small fraction of electrons causing them to move from the valence band to the conduction band.

1.2 Working principles of a solar cell

Solar cells are based on the photovoltaic effect which takes place when an electron in the valence band of a semiconductor material is promoted to the conduction band upon absorption of a photon with energy greater than or equal to the band gap of the material. This electron leaves a hole behind in the valence band and an electron-hole pair is generated. When an external load is applied charges flow in the circuit and current is generated. We will see that

the photocurrent generation in organic semiconductors happens with some important differences.

The basic structure of a photovoltaic device has an active semiconductor layer sandwiched between two conductors. To allow photons to be absorbed by the active material, the first conductor the light passes through has to be transparent to sunlight. If the two conductors have different work functions, an electric field across the active material is created and charges can be generated. In most solar cells additional extraction layers increase the carrier selectivity.

1.2.1 Solar cell parameters

Solar cell characterization is performed by measuring the solar cell's current I as a function of the voltage V and, in such a way, generating the Current-Voltage (IV) curve. An example of an IV curve is reported in Figure 1.1.

An ideal solar cell operates like a diode in parallel with a current source so that the intensity-current relationship is an exponential function given by

$$I_{diode} = I_0 \left(e^{\frac{qV}{kT}} - 1 \right) - I_L, \quad (1.2)$$

with I_0 reverse bias saturation current (or scale current) and I_L light generated current. The sign convention for current and voltage in photovoltaics is that the photocurrent is negative. When no light shines onto the cell, the IV curve resembles the IV curve of a diode ([5], [6]). The current I_L is generated when light is absorbed and, since the power is given by

$$P = IV, \quad (1.3)$$

the solar cell's maximum power can be directly derived from the IV curve. Then, the power conversion efficiency of a cell is given by the ratio of the maximum power generated by the device and the incoming power from the sun

$$\eta = \frac{P_{out}}{P_{in}}. \quad (1.4)$$

Typically, three important parameters are derived from the IV curve:

- The short-circuit current, I_{SC} , which is the current when the voltage is zero across the cell. It depends on the optical properties of the solar cell, absorption and reflection. I_{SC} also depends on the power of the incident light source and the properties of the material: I_{SC} increases with the flux of sufficiently energetic photons but it also decreases with larger energy gaps because in that case the number of absorbed photons

is reduced. Instead of I_{SC} , which depends on the area of the solar cell, the short-circuit current density J_{SC} (mA/cm²) is generally used to avoid this dependence.

- The open-circuit voltage, V_{OC} , is the voltage at zero current when the contacts are isolated. By setting the net current equal to zero in (1.2), the following expression is obtained

$$V_{OC} = \frac{kT}{q} \ln\left(\frac{I_L}{I_0} + 1\right). \quad (1.5)$$

So, V_{OC} increases with the photogenerated current and decreases with the saturation current which decreases with the energy gap and consequently the open circuit voltage increases with the energy gap. Furthermore, since I_0 depends on recombination processes in the solar cell, open-circuit voltage is a measure of the amount of recombination in the device [7].

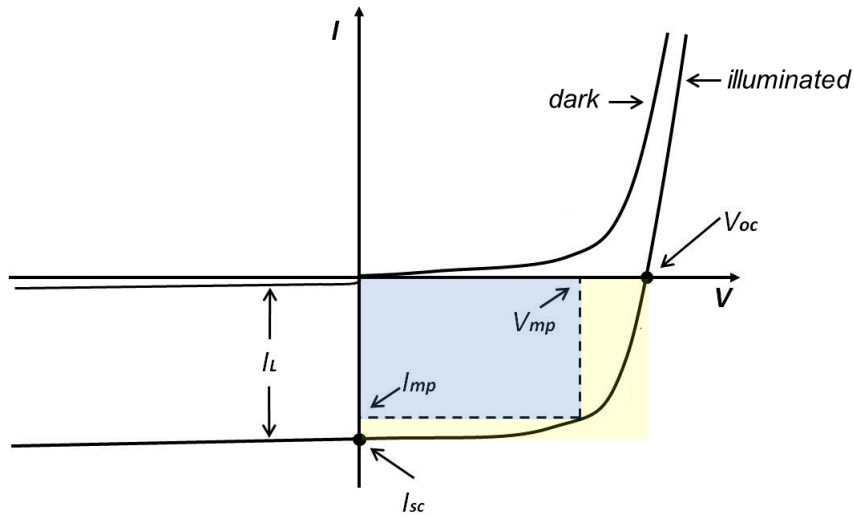


Figure1.1 Intensity-Voltage curve of a solar cell. In the dark the solar cell behaves like a diode. Once illuminated light generated current I_L starts flowing through the device. The short circuit current I_{SC} is the maximum current extracted from the device at $V=0$; the open circuit voltage V_{OC} is the maximum voltage though the device at $I=0$. Their product gives the actual power from the solar cell which is different from product of I_{SC} and V_{OC} . From that difference the fill factor FF is defined as the ratio between the yellow and the blue area.

- The Fill factor, FF , is a parameter which, together with V_{OC} and I_{SC} , determines the maximum power from a solar cell. It is defined as the ratio of the maximum power from the solar cell to the product of V_{OC} and J_{SC}

$$FF = \frac{P_{mp}}{V_{OC} J_{SC}} = \frac{V_{mp} J_{mp}}{V_{OC} J_{SC}}. \quad (1.6)$$

Graphically, the FF is the area of the largest rectangle that will fit in the IV curve compared to the area span by V_{OC} and J_{SC} . Here, $P_{mp} = V_{mp} J_{mp}$ is the maximum power extracted from the solar cell and corresponds to the value at the knee of the IV curve in Figure 1.1

With the help of these parameters the efficiency of a solar cell can be also written as

$$\eta = \frac{P_{mp}}{P_{in}} = \frac{V_{mp} J_{mp}}{P_{in}} = \frac{V_{OC} J_{SC} FF}{P_{in}}. \quad (1.7)$$

1.2.2 Solar spectrum and air mass

Solar radiation closely matches a black body radiator at about 5800 K. The solar spectrum covers ultra violet to infrared wavelength ranges. Only 30% of incident light energy is in the visible light range, while over 50% lies in the infrared range. The photons in UV, visible and NIR range have enough energy to excite electrons in a typical semiconducting material such as silicon, and this can be effectively used for charge generation.

As it passes through the atmosphere, sunlight is attenuated by scattering and absorption by the elements in the Earth's atmosphere. As a consequence, the shape of the solar spectrum changes as it reaches the Earth's surface: the more atmosphere through which it passes, the greater the attenuation. In order to take into account this attenuation the Air Mass is defined as the path length which light takes through the atmosphere normalized to the shortest possible path length (that is, when the sun is directly overhead). It quantifies the reduction in the power and spectrum of light as it passes through the atmosphere and is absorbed by air and dust. The Air Mass is defined as:

$$AM = \frac{1}{\cos\theta}, \quad (1.9)$$

where θ is the angle from the vertical (zenith angle). The Air Mass is 1 when the sun is directly overhead. Being depending on the Sun's elevation path through the sky, the air mass number varies with time of day, with the passing seasons of the year, and with the latitude of the observer. The standard for device testing is AM1.5, which corresponds to a total power density of 100mW/cm² and an elevation angle of 41.81° above the horizon (thus the zenith angle for the sun is 48.19°) [8].

1.2.3 Shockley-Queisser limit

The maximum theoretical efficiency for a solar cell based on a single p-n junction is given by the Shockley-Queisser limit or detailed balance limit (Figure 1.2). This limit is calculated by examining the amount of electrical energy extracted per incident photon.

The calculation made by William Shockley and Hans Queisser places the maximum solar conversion efficiency around 33.7% for a single p-n junction device with a band gap of 1.34 eV and using an AM1.5 solar spectrum [2]. The limit is not predicted on the base of empirical data but actually built up on the basis of the detailed balance principle, which is rooted in the second law of thermodynamics.

The most important factor for the efficiency calculation is the energy gap for photon absorption. Incident photons with energy higher than the energy gap can be absorbed, exciting electrons to higher electronic bands, while those with lower energy are not absorbed, either reflected or transmitted. Moreover, the portion of the absorbed energy greater than the energy gap is dissipated in the process of electron relaxation in form of heat, resulting in further loss of the absorbed energy.

After absorption, not all absorbed energy can be converted into useful power, which is the electrical power in the case of a solar cell. Only the free energy not associated with entropy can be extracted from the device. In the situation of a p-n junction solar cell, this effect manifests itself in the radiative recombination process, the inverse process of photon absorption. Therefore, recombination places an upper limit on the rate of electron-hole production.

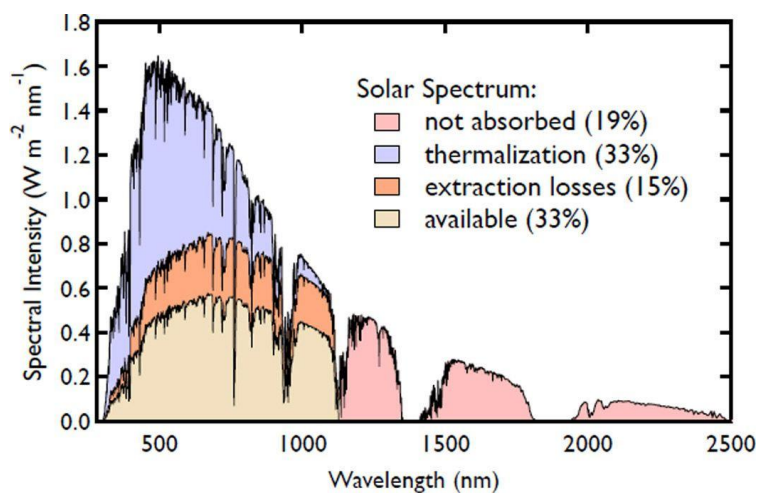


Figure1.2 Shockley-Queisser efficiency limit for a silicon solar cell. Considering silicon absorbing sun light, incident photons with energy lower than the energy bandgap are not absorbed (19%); photons with energy higher than the energy gap will be absorbed, electrons will be excited to the conduction band but the excess of energy will be wasted as well in form of heat as the electrons thermalize (33%). 15% of the incoming power is lost due to extraction losses. As a result, only 33% of the power from the sun is actually converted into usable photocurrent (Figure credit: NREL).

Lastly, at room temperature the solar cell in itself behaves like a blackbody radiator emitting a small percentage of radiation which cannot be captured by the cell.

1.3 Organic semiconductors

Organic semiconductors combine the optoelectronic advantages of semiconducting materials with the chemical and physical properties of organic compounds. Mostly made from carbon and hydrogen, organic semiconductors appear in several molecular structures, with molecular weights varying from hundreds to ten of thousands.

Known organic semiconductors can be broadly classified into two groups on the basis of their molecular weight: small molecules, conjugated compounds of molecular weight less than 1000, and polymers with molecular weight greater than 1000. In the solid state, organic molecules are kept bound by van der Waals forces which decrease as $1/R^6$, where R is the intermolecular spacing, therefore organic materials are typically much softer than their inorganic counterpart which are covalently bonded with strength falling off as $1/R^2$.

1.3.1 Band structure and conductivity

The chemical structure of organic materials is determined by σ -bonds which come from the superposition of the orbitals of the electrons shared between atoms. In the case of single bond C-C, the four valence electrons of each atom form four sp^3 hybridized orbitals. Since the highest electron density is on the nuclear plane, electrons contributing to this kind of bond are strongly localized. As a consequence, the resulting energy difference between occupied binding orbitals and unoccupied anti-binding orbitals is comparably large and molecules only characterized by σ -bonds have insulating properties due to this electron immobility. For a double covalent bond C=C π -bonds is formed: sp^2 hybridization gives a configuration with three planar sp^2 orbitals and a p_z orbital perpendicular to the plane. The lateral superposition of p_z orbitals gives the π -bonds characterized by more delocalized electrons (one electron per p_z orbital) and smaller energy difference enabling absorption and fluorescence in the visible spectral range. Organic molecules presenting carbon chains or rings with both single and double bonds are defined as conjugated systems where the superposition of π -bond orbitals results in electrons delocalized over the whole molecule. In the same way, the anti-bonding orbital π^* is created. π -type bonding and antibonding orbitals define respectively the highest occupied molecular orbital (HOMO) and the lowest unoccupied molecular orbital (LUMO), which can be seen as the equivalent of the valence band and conduction band in the case of inorganic semiconductors. The energy gap between HOMO and LUMO is the energy bandgap E_g and its size defines the lowest-energy transition for the semiconductor. The π - π^* optical transitions often fall into visible spectra range and can be tuned synthetically through molecular design, a feature that make organic semiconductors particularly appealing for optoelectronic applications. Upon absorption of a photon, an electron is excited from the HOMO to the LUMO. A bound electron-hole pair is formed with a binding energy of the order of eV, known as an exciton. Excitons are mobile molecular states which can travel within the solid hopping from molecule to molecule, or in the case of polymers, from chain to chain. Such a high binding energy (in contrast with inorganic materials where the exciton binding energy is only a few mV) is a direct consequence of the low dielectric constant of this class of materials

($\epsilon = 3-4$) which enhances the Coulomb attraction between electron and hole [9]. Owing to this, strong electric fields are needed for exciton dissociation or bound excitons must migrate to an interface where there is a sufficient chemical potential energy drop to drive dissociation into free charge carriers. Consecutively, charge carrier transport can occur via hopping between molecular sites, or from chain to chain. The carrier mobilities are low compared with inorganic semiconductors whose room temperature values typically range from 100 to $10^4 \text{ cm}^2 \text{ V}^{-1} \text{ s}^{-1}$. In contrast the highest mobility value for organic materials is obtained in highly ordered molecular materials and is only $1-10 \text{ cm}^2 \text{ V}^{-1} \text{ s}^{-1}$ whereas for more disordered systems and polymers mobilities are typically $10^{-3}-10^{-5}$ [10].

1.4 Organic solar cells

Organic solar cells (OPV) typically consist of an active layer of organic semiconductor materials sandwiched between two electrodes and possibly other extraction layers. While absorption of a photon in a conventional inorganic solar cell leads to an immediate creation of free charges, the excitonic character of the organic semiconductors leads to the formation of a neutral electron-hole pair with high binding energy. This exciton cannot be dissociated into free charges by the internal electric field within a single layer.

As a direct consequence of such a high exciton binding energy, the standard homojunction device architecture is inefficient and a heterojunction between two materials, an electron donor (D) material (which will also be the active material of the designed solar cell) and an electron acceptor (A) material, needs to be introduced in order to successfully dissociate excitons into free charges. The virtue of a heterojunction interface lies in the difference of chemical potential between D and A responsible for the LUMO-LUMO energy offset which can be high enough to overcome the binding energy and split the exciton into free charges [11], [12], [13].

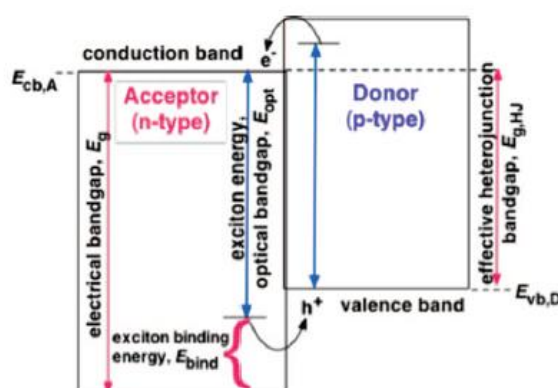


Figure 1.3 Scheme of relevant energies involved in a bilinear heterojunction solar cell [12].

With this architecture the charge generation is a multistep process. Once formed in the donor material, the exciton diffuses towards the D/A heterojunction where the energy offset dissociates the strongly bound exciton into free charges. Initially, excitons at the D/A interface evolve into charge-transfer states, which are bound electron-hole pairs across the junction. Then, the charge transfer states can be dissociated into free charges, which will migrate to the corresponding electrode and are collected to create photocurrent.

If excitons do not reach the interface, they recombine and the absorbed energy is dissipated without generating photocurrent. Hence the thickness of the organic layers plays a crucial role since it needs to be comparable to the exciton diffusion length [14], the average distance that an exciton travels before recombining,

$$L_d = \sqrt{2D\tau} , \quad (1.10)$$

where D is the diffusion coefficient and τ is the lifetime of the exciton. Ideally, the thickness of the organic layers has to be finely tuned allowing for efficient light absorption, which would be favored by thicker layers, and efficient exciton diffusion to the heterojunction, which instead, being the exciton diffusion length usually around tens of nm, is favored by thinner layers.

Another factor limiting the exciton diffusion is trapping. The energy of the excited states can be trapped during the diffusion on non-radiative defect sites always present in thin films. In this respect morphology is critical to achieve high performances in organic photovoltaics. Generally, inhomogeneous regions of the film with a higher trap density show higher rate of quenching and strong quenching is also observed in the vicinity of metal interfaces.

1.4.1 OPV device structures

OPV devices involving a D/A architecture have been intensively studied with the purpose of improving exciton diffusion and dissociation by investigating several geometries. As a result, during the last 20 years a few different device structures have been developed with the objective to make the generation of free charge carriers more efficient.

Organic solar cells can be fabricated in bilayer device architecture where donor and acceptor materials are stacked sequentially and sandwiched between the two electrodes. This planar geometry is unfortunately limited by the small exciton diffusion length of the donor (or acceptor) which requires ultra-thin active layers usually only tens of nanometers thick. Hence, bilayer OPV cells collect only small amounts of photons.

To overcome the problem related to the small diffusion length typical of the organic active materials, a bulk heterojunction geometry has been introduced. The idea of a bulk heterojunction is to blend the donor and acceptor materials so that an absorbing site is always within an exciton diffusion length of an interface. This structure allows for thicker active region, around 100 nm, and has the potential for high efficiency, but on the other side bulk heterojunction devices are very sensitive to morphology changes as isolated domains can trap

charges, hence leading to recombination [11]. Furthermore, in blend OPV holes and electrons travel long distances before reaching an electrode which also increase the risk of charge recombination and exciton-charge recombination. In addition, the blend layer contains discontinuous islands of one material so that generated charges in the islands cannot be collected at an electrode.

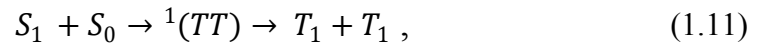
To overcome the charge recombination problem of the blend OPV cell and maintain efficient exciton dissociation nanostructured OPV cells were designed [15]. In this design donor and acceptor are blend together in a periodic structure which allows for a high morphology control. This patterned structure is able to maximize exciton dissociation as long as the pattern period is comparable with the exciton diffusion length. At the same time, the height of the pattern is tuned to absorb enough photons without losing charges by recombination.

1.5 Singlet fission process

Singlet exciton fission is a spin allowed process occurring in some conjugated materials where a singlet exciton state (spin=0) spontaneously splits into two triplet excited states (spin=1), each one carrying half the energy of the singlet exciton.

Triplets cannot be directly created by absorbing a photon, therefore, upon light absorption, a photogenerated singlet exciton (S_1) couples to a nearby chromophore in the ground state (S_0). The first molecule relaxes to a lower-energy triplet state (T_1) and transfers energy to the second coupled molecule, which is excited to a triplet state (T_1).

In a system involving a molecule in its first excited state and a second molecule in its ground state, the kinetic scheme for the singlet fission process is given by



which describes the process as a two-step process. First, the conversion of the initial singlet states S_1 and S_0 into a pair of correlated triplets ${}^1(TT)$ takes place and this coupled state is localized over neighbouring chromophores with overall spin zero. Then, the dissociation into free triplets happens.

A two-molecule system is described by a total Hamiltonian which is the sum of two parts

$$H_{tot} = H_0 + H_{int}. \quad (1.12)$$

Here H_0 is the non-interacting part describing the behaviour of each single chromophore in isolation and H_{int} is the interaction Hamiltonian. The singlet fission is induced by H_{int}

$$H_{int} = H_{el} + H_{sp}. \quad (1.13)$$

Here, H_{el} is the spin-free electrostatic part which describes the behaviour of the electrons. It affects the rate of singlet fission as a function of the molecular structure and is responsible for the conversion of the initial singlets into the correlated triplet pair. H_{sp} is the spin-dependent

part responsible for the eventual dissociation into free triplets. Since the common organic molecules do not contain heavy atoms hyperfine interaction with nuclear magnetic moments and the spin-orbit coupling are negligible terms and H_{sp} is mainly constituted by the spin dipole-dipole interaction and the Zeeman interaction with an outside magnetic field.

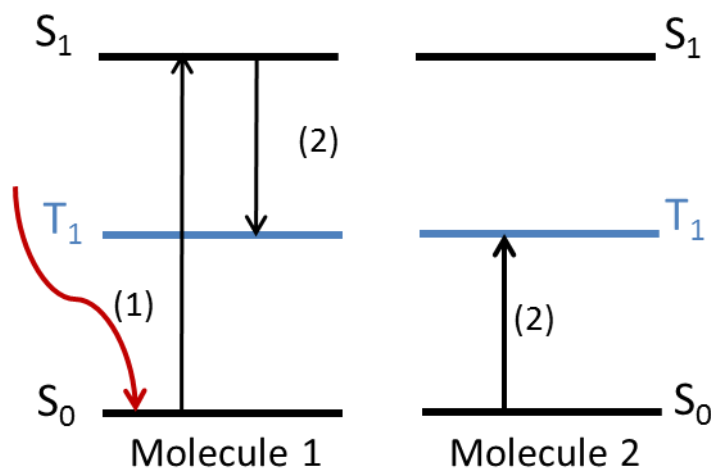


Figure 3.4 Schematic sketch of the singlet fission process. The first molecule absorbs a photon and a singlet exciton S_1 is created (1). The photogenerated singlet exciton couples to a nearby molecule in its ground state S_0 transferring part of its energy to it (2). The exciton is converted into two triplet excitons T_1 each carrying half of the energy of the singlet [18].

Singlet fission can be a very efficient and fast process occurring also on subpicoseconds scale, as in the case of tetracene and pentacene, the most widely studied singlet fission materials [16], [17]. Nevertheless, for dissociation into free triplets the interaction between the two chromophores needs to be in a certain range of strength: if the coupling between the molecules is too weak there will be no formation of the correlated triplet pair on timescales fast enough to compete with other relaxation events such as fluorescence; on the other hand, a coupling significantly stronger than kT does not allow for fast dissociation of the $^1(TT)$ state and the system behaves like a single chromophore [18], [19].

Singlet fission can be observed through delayed and prompt fluorescence: the generated singlet excitons can either recombine radiatively resulting in prompt fluorescence, or they can undergo the competing process of fission to form triplets. The prompt fluorescence yield is inversely proportional to the rate of singlet fission. On the other hand, delayed fluorescence is emitted when two triplets T_1 recombine to one singlet S_1 which then emits fluorescence. To detect singlet fission the Merrifield approach can be used [20], [21], [22]. The model assumes that the probability of recombination of two T_1 followed by fluorescence is proportional to the number of triplet-pair levels with singlet character. Applying a magnetic field alters the number of triplet pair states that can become singlets. Now, a distinction needs to be made between low field and high field. At low field three pair states have singlet character, while in high field regime the number of triplet pair states that can become singlets is reduced from

three to two via Zeeman interaction and this leads to a decrease of the process for both singlet fission and triplet fusion.

In simple words, in the low-field regime we have a higher population of singlet states that can undergo singlet fission with respect to the high field regime. This, of course, exert a profound effect on the fluorescence rates: first the rate of delayed fluorescence coming triplets recombination increases at low field and then decreases down to a saturation point at high field; consequently the prompt fluorescence will decrease at first and then increase as a sign that the population of triplets has reduced and the fluorescence is due to singlet recombination. The Merrifield approach is used in photovoltaics to test whether the photocurrent originates from triplet excitons generated via singlet fission: the increase in prompt fluorescence at high field corresponds to a decrease in photocurrent if this originates from triplets.

1.5.1 Singlet fission in photovoltaics

The singlet fission process was firstly studied with the purpose of finding the mechanism behind the unusual magnetic field dependence of the photoluminescence of crystalline anthracene [23]. During the 60s and 70s it was studied stayed mainly on a fundamental level and theoretical formulations were developed [21], [24], [25]. The first suggestion for using singlet fission material in solar cells already appeared in 1979 [26] but except from this brief appearance in literature, singlet fission has seen little attention for almost thirty years.

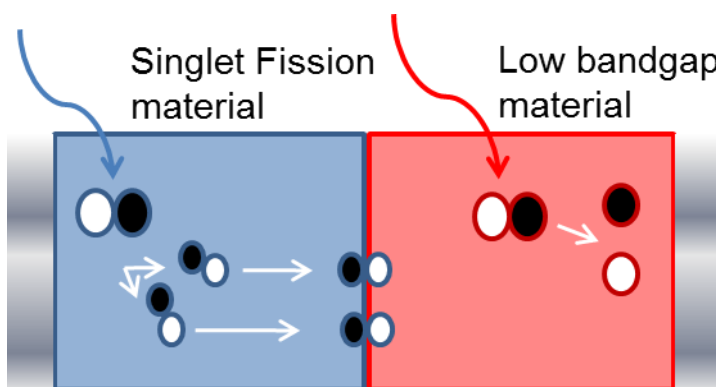


Figure 1.5 Scheme of a general two-bandgap solar cell coupling a singlet fission high-bandgap material with a low-bandgap material. Low energy photons generate directly photocurrent in the low-bandgap material, while high energy photons are absorbed in the singlet fission material where they are converted into two triplets which will then separate and free charges can be collected at the respective electrodes.

Today's interest in singlet fission was triggered in 2006 when detailed balance calculation showed that singlet fission has the potential to rise the Shockley-Queisser limit from 34% to

44% provided that $S_0-S_1 \geq 2$ eV and the triplets are all successfully separated into free charges for a triplets yield of 200% per absorbed photon [3]. It needs to be noted that singlet fission alone does not improve solar cell performances because while photocurrent can be doubled, at the same time the photovoltage is roughly halved due to the lower energy of the triplets. As a consequence, extracted power given by the product of IV is not improved. The real improvement comes from the coupling of the singlet fission material with a low bandgap material which acts both as electron acceptor and as low energy photon absorber.

Figure 1.5 shows a general scheme of such a two-bandgap device: low energy photons generate directly photocurrent in the low-bandgap material, while high energy photons are absorbed in the singlet fission material which will undergo singlet fission generating two triplets per incoming photon which will be separated into free charges at the interface and finally collected at the respective electrodes. This way, more of the solar spectrum is used in the process of producing power.

1.5.2 Singlet fission materials

At the beginning singlet fission was only known to happen in molecular crystals. In particular polyacenes, consisting of fused acene rings, were common materials for SF studies. Generally, it is experimentally found that the generation of two triplets from a singlet states becomes less and less endothermic as the molecular length increases.

Anthracene is the shortest member of the polyacenes family capable of undergoing singlet fission and also the first one to be studied in 1968 [23]. In anthracene crystals the process is endoergic as there is an energy deficit of 0.53 eV between $E(S_1) = 3.13$ eV and $2E(T_1) = 3.66$ eV ([27], [28]) which is larger than kT at room temperature and can be provided optically. Further, crystalline anthracene has a fluorescence yield of 95% [29] which shows that singlet fission is not competitive at room temperatures.

Tetracene is one of the most thoroughly studied molecular crystal in which singlet fission is still endoergic, but with a lower energy deficit than anthracene $2E(T_1) - E(S_1) = 0.16$ eV. Femtosecond transient absorption in combination with picosecond fluorescence revealed that the initially excited singlet state relaxes with a decay time of 80 ps with the formation of the dark $^1(TT)$ states within the first 100 ps [31]. This fast conversion, despite the energetic mismatch stems from the increase in entropy during singlet fission. Tetracene represents an ideal singlet fission candidate for photovoltaics applications because it absorbs at $\lambda < 550$ nm producing triplet excitons with energy $E(T_1) = 1.2$ eV, close to the ideal bandgap of 1 eV required for highly efficient, two-bandgap solar cells exceeding the Shockley-Queisser limit. Further, a long triplet diffusion length has been measured in crystalline tetracene [32]. However, because the singlet fission process in tetracene is slightly endoergic, the inverse process of triplet-triplet annihilation to a singlet exciton is also favored resulting in lower singlet fission rate. Nevertheless, tetracene singlet fission solar cells have been fabricated, both in one-bandgap Tetracene/ C_{60} structure ([33], [34]) and two-bandgap

Tetracene/CuPc/C₆₀ architecture using copper phthalocyanine (CuPc) as triplet transfer layer and IR absorber [35].

Pentacene is the shortest linear polyacene molecule for which singlet fission is an exoergic process: $E(S_1) = 1.83$ eV and $2E(T_1) = 1.62$ eV ([36], [37]). Singlet fission in pentacene has been observed occurring very efficiently at rapid timescale of 80 fs through the formation of the intermediate $^1(TT)$ state ([16], [38]). The ultrafast nature of singlet fission in pentacene makes it a strong candidate for photovoltaic devices because singlet fission can outcompete decay channels such as singlet exciton dissociation into charge. The first efficient pentacene solar cells exhibited high external and internal quantum efficiency both in bilinear ([39], [40]) and bulk heterojunction architecture ([41], [42]). Marc Baldo's group at MIT fabricated Pentacene/Fullerene devices with external quantum efficiency (number of electrons per incoming photon) EQE > 100% [43], [44]. With the purpose of increasing solar cell efficiencies, two-bandgap Pentacene/Nanocrystals devices were realized in Richard Friend's group [45], [46], [47], in particular [47] reported a two-bandgap solar cells using a soluble derivative of pentacene, TIPS-pentacene.

Singlet fission has also been observed with high triplet yields in rylene derivatives ([48], [49]), in polymers but generally with very low triplet yield [17] and suggested to occur in rubrene crystals [50].

1.6 Motivation

As a consequence of this potential application in photovoltaics technology, research on singlet fission based solar cells has intensively increased over the last 5 years. However, pentacene is well known for its high instability in light and air which makes it not suitable for PV large-scale applications. Stability of Pentacene/Fullerene devices was studied under 70 minutes of constant illumination both in air and in vacuum. For air exposed devices photocurrent is observed dropping to almost half its original value already after 20 minutes while the efficiency is reduced rapidly to less than 10% its original value within the first 40 minutes [51]. Such an important drop in device performances is due both to an oxygen induced degradation, leading to a decrease in absorption and disruption of the crystal network ([52], [53], [54]), and to a less effective photo-induced degradation [55].

These stability issues with pentacene, which is the most famous and widely used singlet fission material in PV technology, motivate research for more stable, PV suitable singlet fission materials. In this regard, a valid alternative to pentacene is offered by terrylene, the longer analogue of perylene, a molecule belonging to the rylene hydrocarbon family. Rylene derivatives are well known for exhibiting relatively high electron affinity and mobility together with excellent chemical, thermal and photochemical stability. Terrylene molecule in particular has high extinction coefficient, high fluorescence quantum yield and, in addition, it can also be made so cheap and stable that, in some derivatives, it is used as the main component of car paint.

Here we fabricate solar cells with a newly synthesized terrylene derivative suitable for solution process application, 2,5,10,13-tetra(*tert*-butyl)terrylene (*t*-butyl-Tr). Studies on deposited thin film proved this new terrylene derivative undergoing efficient singlet fission with rapid triplet formation within 120 ± 20 ps from the singlet formation and with a triplet yield of $170 \pm 20\%$ strongly depending on the crystallinity of the film. Relevant states for singlet fission in *t*-butyl-Tr resulted at nearly ideal energies: $E(S_1) = 2.29$ eV, $E(T_1) = 1.1$ eV and $E(T_2) = 2.33$ eV. Therefore, besides the favorable molecular packing, the efficiency of the process is due to the fact that both requirements for generating a high triplet yield are satisfied: $E(S_1) \geq 2E(T_1)$ ensures that singlet fission is thermodynamically spontaneous and $E(T_2) > E(S_1)$ suppresses triplet-triplet annihilation [49]. Devices were fabricated in bilayer structure because, as already observed for tetracene and pentacene, in singlet fission solar cells the photocurrent (and therefore the triplet yield) will be maximized for a certain thickness of the fission layer after which losses will become significant [63].

Another key reason for choosing *t*-butyl-Tr is that the energy of the triplets $E(T_1) = 1.1$ eV finely matches silicon bandgap which is the dominating solar technology, so in the long run this material might be used as a singlet fission sensitizer for silicon solar cells.

Chapter 2

Experimental methods

This chapter describes the experimental methods used to achieve the results presented in Chapter 3. First the fabrication of devices with two different architectures is presented: one-bandgap t-butyl-Terrylene/Fullerene devices and a version replacing Fullerene with PbS nanocrystals realizing a two bandgap device. Device fabrication is then followed by a description of the characterization techniques used to evaluate solar cell performance.

Material	Short name	Details
<i>One-bandgap device</i>		
Bathocuproine	BCP	99,99%
Fullerene	C ₆₀	99,9%
Indium TearnOxyde	ITO	-
Poly(3-hexylthiophene-2,5-diyl)	P3HT	Regioregular
Poly(3,4-ethylenedioxythiophene) polystyrenesulfonate	PEDOT:PSS	
2,5,10,13-tetra(tert-utyl)terrylene	t-butyl-Tr	NWU sythesis
Silver	Ag	99,999%
<i>Two-bandgap device</i>		
Gold	Au	99,999%
Lead sulfide	PbS	Home-synthesis
Molybdenum trioxide	MoO ₃	99,97%
Titanium dioxide	TiO ₂	99,999%
<i>TiO₂ solution</i>		
Ethanol (anhydrous)		-
Hydrochloride	HCl	2M
Titanium(IV) isopropoxide	TTIP	99,999%
<i>PbS quantum dots synthesis</i>		
Lead oxide	PbO	99,999%
Trimethylsilyl sulfide	TMS	98%
Octadecene	ODE	90%
Oleic acid	OA	99%
<i>Solvents and others</i>		
Acetone	-	-
Acetonitrile (anhydrous)	ACN	98,8%
Benzene-1,3-dithiol	BDT	99%
Chlorobenzene (anhydrous)	-	98,8%
Isopropanol	IPA	-
Octane (anhydrous)	-	99%

Table 1. Table of the materials used for device fabrication.

2.1 One-bandgap device fabrication

For the one-bandgap device fabrication we started from ref [44] where pentacene is used as singlet fission material in a well optimized architecture. Solar cells were fabricated on pre-patterned ITO covered glass substrates. The thickness of the ITO was 150 nm. Substrates were cleaned by sonication in Micro90 detergent solution, deionized water, acetone and IPA for 10 minutes each. After being nitrogen dried, substrates were cleaned with oxygen plasma in a plasma cleaner with the purpose of make the ITO surface hydrophilic and to remove organic residuals.

The aqueous dispersion of PEDOT:PSS, a conductive polymer widely used in organic photovoltaics for its high conductivity, high stability and good thin-film transparency [56], was filtered through a 0.45 μm PVDF filter and spun on the pre-cleaned substrates in air at 4000 rpm for 60 seconds for a final thickness of 38 nm. The substrates were then annealed at 135 $^{\circ}\text{C}$ for 20 minutes in nitrogen atmosphere inside the glovebox (O_2 and H_2O levels less than 0.5 ppm).

In some cases P3HT was also introduced into our device architecture as both hole-transporting layer and triplets-blocking layer. P3HT was dissolved in chlorobenzene inside the glovebox at a concentration of 4mg/mL, heated and stirred for 30 minutes at a temperature of 60 $^{\circ}\text{C}$. After fully dissolved, P3HT was filtered through a 0.2 μm PTFE filter and spun onto the PEDOT:PSS pre-coated substrates for 60 seconds at 2000 rpm for a thickness of 8 nm. Substrates were then annealed at 110 $^{\circ}\text{C}$ for 20 minutes.

All the other layers were evaporated in high vacuum at pressure less than 10^{-7} Torr. Following studies on singlet fission in thin film *t*-butyl-Tr [49], the latter was evaporated at a rate of 2 $\text{\AA}/\text{s}$. C_{60} as electron acceptor, BCP as hole blocking layer and Ag as back electrode were evaporated at a rate of 1 $\text{\AA}/\text{s}$ with final thicknesses of 35, 15 and 100 nm respectively.

Figure 2.1 a) and b) report the final device architecture with relative energy levels and finally Figure 2.1 c) shows a picture of the device.

2.2 Two-bandgap device fabrication

Two-bandgap devices with PbS nanocrystals as electron acceptor and IR absorber were fabricated following Le Yang's work [47] in an inverted structure (with the light passing through the acceptor first).

PbS synthesis Due to the quantum confinement, it is possible to vary the bandgap of the nanocrystals by varying their size [57]. Nanocrystal size can be finely tuned by varying the reaction time and the injection temperature. PbS nanocrystal synthesis was performed by Le Yang following the hot injection method described in [47]. The reaction mixture was prepared by dissolving PbO (2.0 mmol, 0.45 g) and OA (4.73 mmol, 1.5 mL) in ODE (62.5 mmol, 20ml) and then degassed under vacuum at 100 $^{\circ}\text{C}$. The sulfide precursor was prepared by

dissolving TMS (1.0 mmol, 213 μL) and DPP (0.060 mmol, 104 μL) in pre-degassed ODE (31.25 mmol, 10 mL; the precursor was then injected rapidly into the reaction mixture at a temperature 120-170 $^{\circ}\text{C}$ in nitrogen atmosphere. The heating mantle was removed and the solution was then allowed to cool down to 35 $^{\circ}\text{C}$. Purification steps were performed in nitrogen and consisted of repeated cycles of dissolving in toluene and precipitation with ethanol and butanol/methanol mixture. Finally PbS nanocrystals were dissolved in octane for spinning.

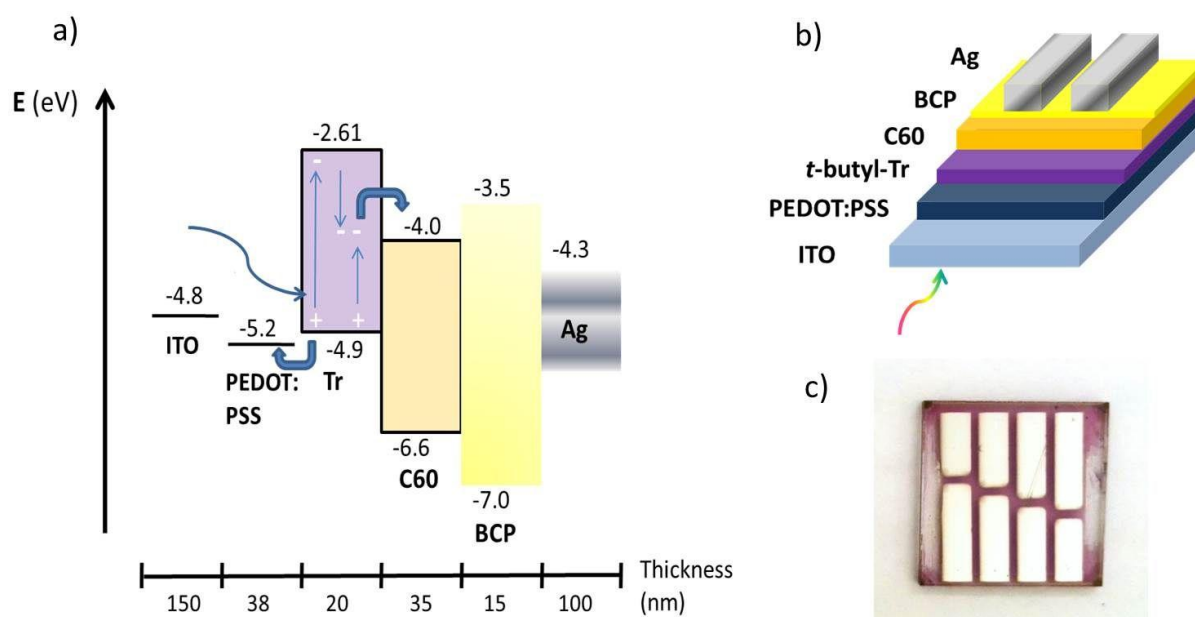


Figure 2.1 Device architecture and energy levels for a one-bandgap device. a) Device architecture of a one-bandgap *t*-butyl-Tr solar cell with thicknesses and energy levels for each layer. Light is incident from the ITO. In the *t*-butyl-Tr layer excitons will undergo singlet fission, created triplets will diffuse to the interface *t*-butyl-Tr/ C_{60} where the chemical potential will overcome their binding energy and separate them into free charges. Charges will then be collected at the respective electrode: electrons will proceed to the Ag/BCP cathode and holes will transfer to the ITO/PEDOT:PSS anode. b) Sketch of a one-bandgap *t*-butyl-Tr device. c) Photograph from the Ag electrode of a one-bandgap *t*-butyl-Tr device where each of the eight pixels is an individual solar cell.

TiO₂ solution: The electron transporting TiO₂ was prepared in solution by a sol-gel method [58]. Dry ethanol (21.4 mmol, 1.25 mL) and 2 M HCl (0.35 mmol, 17.5 μL) were mixed in a solution (1). Titanium solution was prepared by mixing TMP TiO₂ (0.60 mmol, 175 μL) and dry ethanol (21.4 mmol, 1.25 mL) to form (2). Then, (1) and (2) were mixed together in a 1:1 ratio which was left stirring for 10 minutes.

Device fabrication ITO substrates were cleaned as explained previously. TiO₂ solution was first filtered through a 0.45 μm PVDF filter and then spun at 2000 rpm for 40 seconds. Substrates were then baked in air at 500 $^{\circ}\text{C}$ for 30 minutes. The temperature was set in such a way to increase of 30 $^{\circ}\text{C}$ every 15 minutes.

Substrates were then transferred inside the glovebox in nitrogen atmosphere for the PbS quantum dots spin coating which was performed following the layer-by-layer method previously reported in [59]. A solution of crosslinker ligand BDT was prepared in ACN at a concentration of 1.0 $\mu\text{L/mL}$, the BDT solution was spun onto the TiO_2 -covered substrates with the purpose of functionalizing the surface in order to make the PbS quantum dots attach to it. Excess BDT was washed off with ACN. Each PbS quantum dots layer was created by spin-coating the PbS nanocrystal/octane solution at a concentration of 25 mg/mL. BDT solution was again spun onto the PbS layer as a crosslinker. Excess of BDT was removed by spinning ACN three times and then oleic acid and unattached quantum dots were removed by spinning octane. Every solution was filtered and every spinning was performed at 1500 rpm for 10 seconds after a 5 seconds soaking. The estimated final thickness for a single PbS layer is 15 nm [47]. This cycle was repeated four times for a final thickness of around 60 nm.

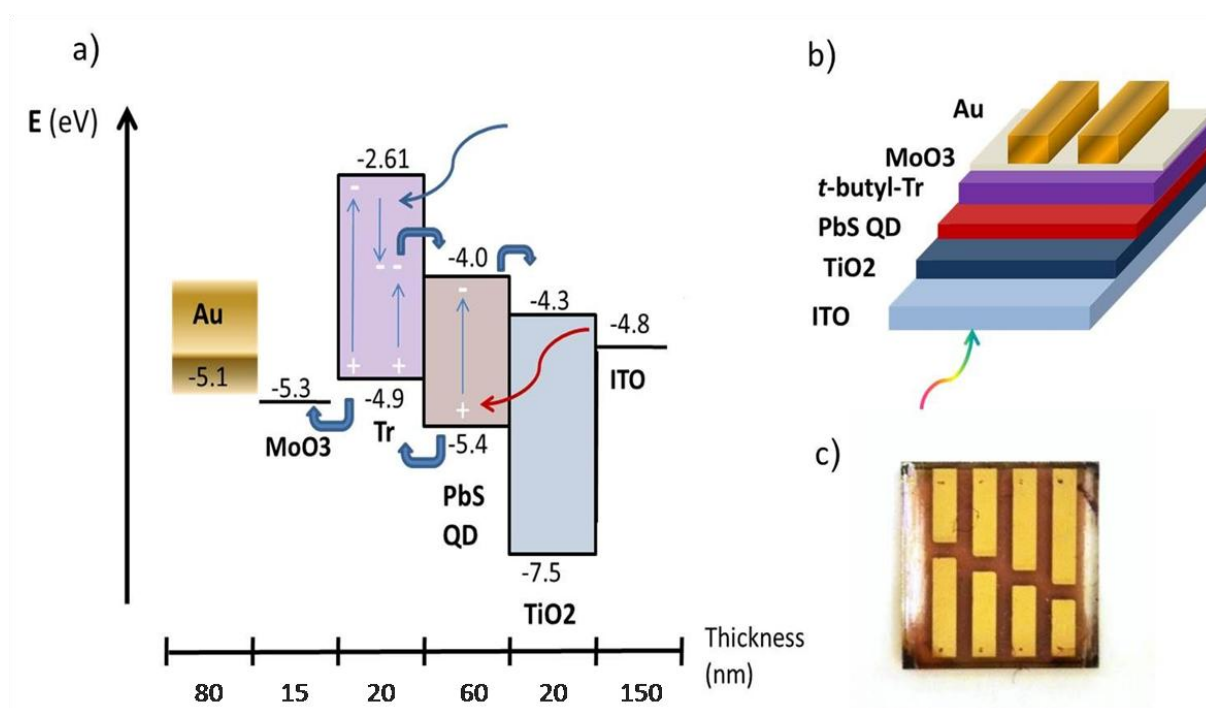


Figure 2.2 Device architecture and energy levels of a two-bandgap device. **a)** Device architecture of a two-bandgap *t*-butyl-Tr/PbS QDs solar cell with thicknesses and energy levels for each layer. Light is incident from the ITO passing through the quantum dots layer first. Low energy photons excite electrons creating direct photocurrent from the PbS, while high energy photons are absorbed in *t*-butyl-Tr which undergoes singlet fission generating enhanced photocurrent. The triplets created will then separate into free charges at the *t*-butyl-Tr/PbS QD interface so that electrons will be collected at the ITO/ TiO_2 cathode and holes at the Au/ MoO_3 anode. **b)** Sketch of a two-bandgap *t*-butyl-Tr/PbS QD device. **c)** Photograph from the Au contact of a two-bandgap *t*-butyl-Tr/PbS QD device where each of the eight pixels is an individual solar cell.

20 nm of *t*-butyl-Tr were deposited on top of the PbS layer by thermal evaporation with the same condition as for the one-bandgap device. Finally, 15 nm of MoO₃ and 80 nm of Au as top electrode were evaporated at a rate of 1 Å/s.

In Figure 2.2 the device architecture, energy levels and real device for the inverted two-bandgap *t*-butyl-Tr/PbS QDs solar cell device are shown.

2.3 Deposition techniques

Spin-coating Solution processable materials were spun onto substrates with two different spin-coaters: a POLOS spin-spin coater kept in air and a G3P SPINCOAT kept in the glovebox were used depending on the sensitivity of the materials to air and solvent used.

Thermal evaporation Evaporation of small molecule organic semiconductors, metal oxides and metals was done with an Angstrom Engineering AMOD evaporator directly attached to the glovebox. The evaporator allowed for the deposition of six different materials at a time. Samples were positioned up-side-down on a sample holder and then loaded in a rotating stage. Layer thickness was measured by Fizeau sensors directly mounted above the evaporating source inside the vacuum chamber and then correcting the layer thickness deposited at the stage by the so called tooling factor, which accounts for the difference of nanometers of deposited material between the thickness sensor and the stage. All tooling factors were calibrated by measuring the deposited thickness via step measurement using the AFM.

2.4 Characterization techniques

UV-Vis Spectroscopy Absorbance of *t*-butyl-Tr and PbS QDs was measured with a Perkin Elmer UV/Vis/NIR spectrometer. A 25 nm layer of *t*-butyl-Tr was evaporated on a bare glass substrates and its absorbance was measured by scanning light in the wavelength range between 300 nm and 700 nm. PbS QDs' absorbance was measured keeping quantum dots in solution inside a cuvette and scanning light in the range between 300 nm and 1200 nm.

Ultraviolet Photoelectron Spectroscopy (UPS) UPS measurements were done to estimate the HOMO energy level of *t*-butyl-Tr. A 25 nm thick layer of *t*-butyl-Tr was evaporated onto Si substrate/Cr (4 nm)/Au layer(50 nm). After evaporation the sample was sealed in nitrogen for shipment. The measurement was done by Marcus Böhm at Cavendish Laboratory, University of Cambridge.

Current-Voltage (IV) measurement IV measurements were performed connecting the two electrodes to a probe station and measuring the current flowing through the device under the illumination of 1 sun (solar spectrum simulator ORIEL SOL2A). In order to prevent any exposure of samples to air which can degrade solar cells performances very easily, devices were loaded in nitrogen atmosphere into a contacted sample holder and kept sealed during the whole measurement, as illustrated in Figure 2.3.

External Quantum Efficiency (EQE) measurement EQE was measured in a home-built optical set up by illuminating solar cells with a laser scanning over different wavelengths and recording the amount of photocurrent at each wavelength. The sample was loaded into the sample holder shown in Figure 2.3 and then mounted on a piezoelectric stage. Single pixels on each sample were then illuminated by a supercontinuum laser (Fianium WL-SC-400-4) tightly focused on the sample through an ultra-long working distance microscope objective. The laser covered a total range of scanning wavelengths from Vis to NIR (between 400nm and 1200 nm), but measurements in the two parts of the spectrum had to be done separately by selecting the appropriate Vis or NIR filter (Fianium AOTF Crystal Technologies).

A beam splitter positioned between the laser source and the sample split the beam into two beams directed to the sample and to a beam monitor which is used as a reference of the incident laser power. The measurement was done by recording EQE from each pixel on the sample. Calibration was done by illuminating a photodiode and recording the respective EQE. EQE for solar cells was calculated as the difference between the signal from the calibrating photodiode and the signal from the sample.

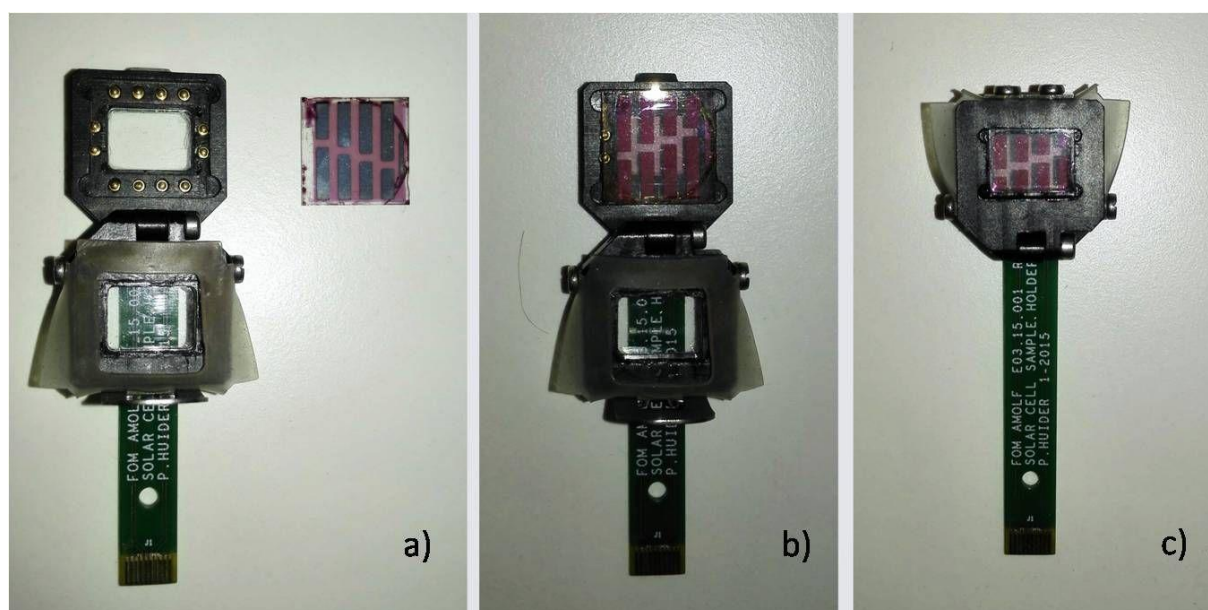


Figure 2.3 Home-built sample holder for device characterization. a) The sample holder has 12 contacts: 8 of them are connected to the 8 Ag contacts, the remaining 4 are connected to the ITO. b) Samples were placed up-side-down in the sample holder inside the glovebox and c) sealed in nitrogen for the measurement.

Atomic Force Microscope (AFM) Atomic Force Microscopy was done with a Veeco Dimension 3100 AFM with subnanometer resolution. AFM scanning was performed to estimate the thickness of layers of materials deposited both via spin/coating and thermal evaporation on glass substrates. The estimation of the thickness was done scanning with the nanometer size probe over a line pre-scratched on the surface of the material. The scratch was

done with tweezers paying attention not to scratch the glass underneath and the thickness was calculated as the difference in height between the material and the substrate. AFM was also used to study morphology of the *t*-butyl-Tr layer.

Chapter 3

Results

In this chapter performance of solar cell are reported. The chapter is divided into two main parts. The first part focuses on one-bandgap devices as the starting point of the project, here failed and successful results are reported. Data collected on two-bandgap devices will be described in the second part of the chapter.

3.1 One-bandgap device with P3HT as triplet blocking layer

As device architecture we decided to keep P3HT as triplet blocking layers between the ITO/PEDOT:PSS anode and the *t*-butyl-Tr layer, as in Congreve's work [44]. A first batch of devices was fabricated varying the thickness of the *t*-butyl-Tr between 20 nm and 40 nm to estimate the diffusion length of the material, which was unknown.

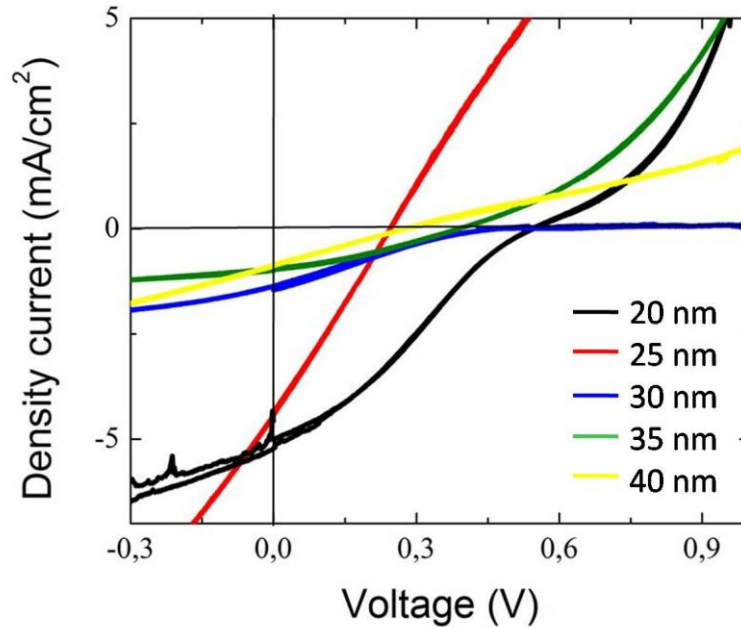


Figure 3.1 IV curves for one-bandgap devices with P3HT as triplet blocking layer and different *t*-butyl-Tr layer thickness. Density current decreases with increasing layer thickness while the open circuit voltage is generally high over the whole scanning range of thickness with the exception of 25 nm.

Experimentally we found that J_{SC} decreases for thicker layers, as it can be seen in Figure 3.1, therefore we deduce that the diffusion length for *t*-butyl-Tr must lie between 20 nm and 25 nm (or even less), as already expected for organic materials. V_{OC} was generally encouragingly high already at the first attempt: detailed balance calculation shows that for bandgap of 1 eV (as determined by the triplet energy) unavoidable of recombination leads to a maximum achievable $V_{OC} = 0.8$ eV.

t-butyl-Tr contribution to the measured photocurrent was confirmed by the external quantum efficiency (EQE) spectrum. EQE is given by the amount of extracted charge carriers divided by the number of incident photons with a certain energy absorbed. Hence, EQE spectra are particularly sensitive to the absorption spectra of layers across the device. We performed the measurement with the method described in section 2.3 and, indeed, we found actual current at the peak of absorption of *t*-butyl-Tr (Figure 3.2).

However, IV curves in Figure 3.1 generally show an “S-shape” which is symptom of an energy barrier due to a non ideal energy level matching in our device structure. With the purpose of improving the device performances, we tried different stage of annealing on the *t*-butyl-Tr layer. On the base of what experimentally suggested in Figure (3.1), 25 nm was chosen as thickness for the singlet fission layer.

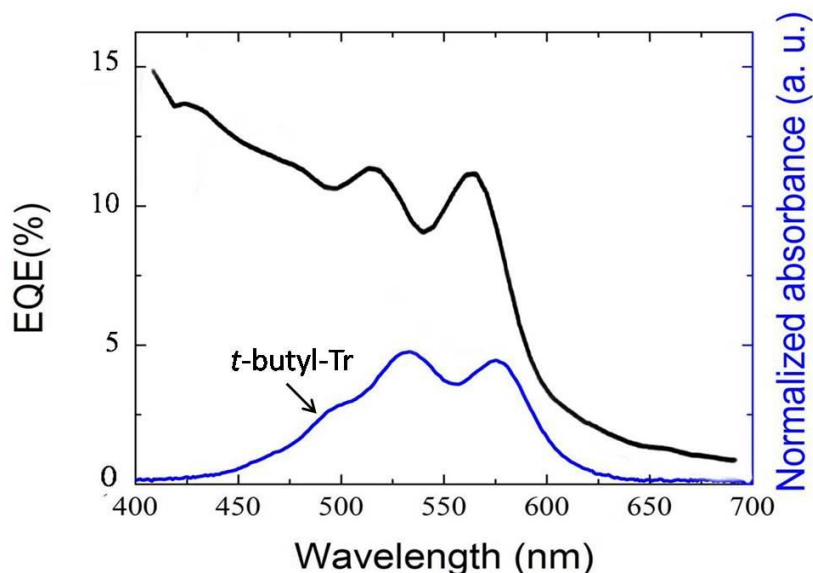


Figure 3.2 EQE spectrum an one-bandgap device with P3HT as hole blocking layer. EQE spectrum for a 30 nm thick *t*-butyl-Tr layer. EQE resembles *t*-butyl-Tr absorption spectrum and, therefore, showing photocurrent coming from the singlet fission layer.

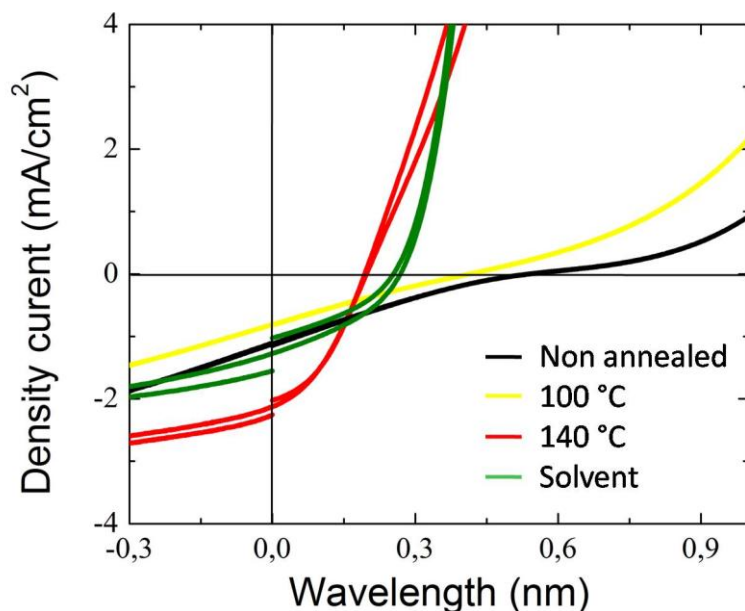


Figure 3.3 IV curves for one-bandgap devices with P3HT as triplet blocking layer for different annealing treatments. 100 °C annealing temperature (yellow) does not exert

sensitive change in solar cell performances if compared with the reference, non annealed *t*-butyl-Tr layer (black). For 140 °C annealing temperature (red) and solvent annealing (green) J_{SC} and FF are improved but at the same time V_{OC} is reduced.

After deposition, samples were baked at 100 °C for 10 minutes and at 140 °C for 6 minutes. Further, a 2 hours toluene solvent annealing was tried on the base of studies on *t*-butyl-Tr thin film which show an improvement of the triplet yield in solvent annealed films due to a higher crystallinity [49].

Unfortunately, annealing revealed not to be ideal for our device. Figure 3.3 shows IV curves for the different annealing treatments compared to the reference, non-annealed layer. A temperature of 100 °C does not seem to affect the solar cell performance and IV curves are still characterized by an energy barrier. On the contrary, 140 °C and toluene annealing give slightly higher J_{SC} and better FF, but at the same time the V_{OC} is strongly reduced.

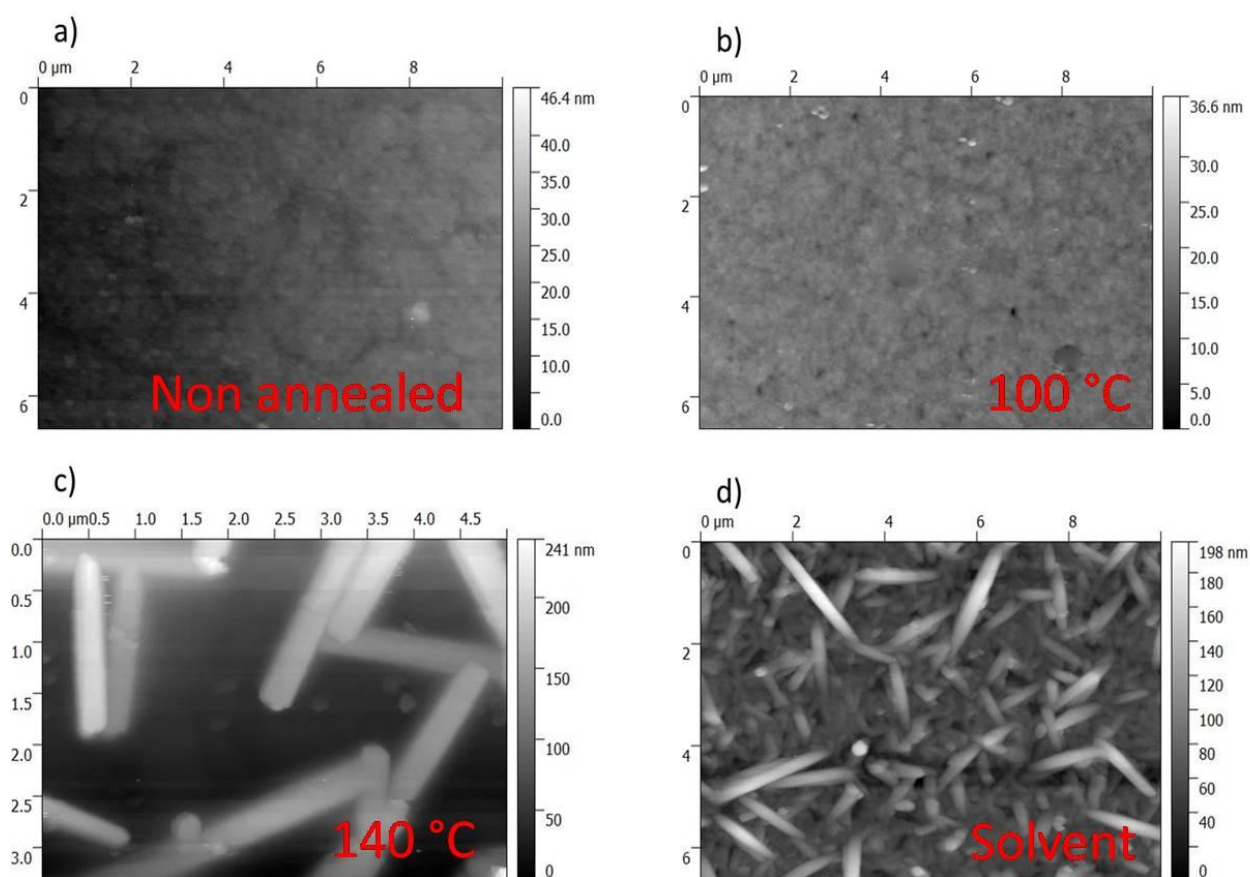


Figure 3.4 AFM pictures of the solar cell surface after different *t*-butyl-Tr annealing treatments. **a)** not annealed and **b)** 100°C/10 minutes annealed samples do not differ significantly in morphology. **c)** 6 minutes at 140 °C brought the material to cluster in big structures of hundreds of nanometers length. **d)** 2 hours toluene annealing brought yields similar crystallization.

AFM studies suggested a tight correlation between device performance and morphology of the singlet fission layer. From Figure 3.4 a) and b) we can see that there is no difference in morphology between the reference, non-annealed sample and the one annealed at 100 °C, a behavior reflecting what we already found in terms of solar cell performances. However, as we increase the temperature up to 140 °C, morphology changes radically and the material clusters in big, long structures (Figure 3.4 c)). We found a similar cluster formation also for toluene annealing (Figure 3.4 d)). Our data suggest that these morphological changes lowered solar cell performances potentially due to incomplete film coverage and feature sizes exceeding the diffusion length in *t*-butyl-Tr.

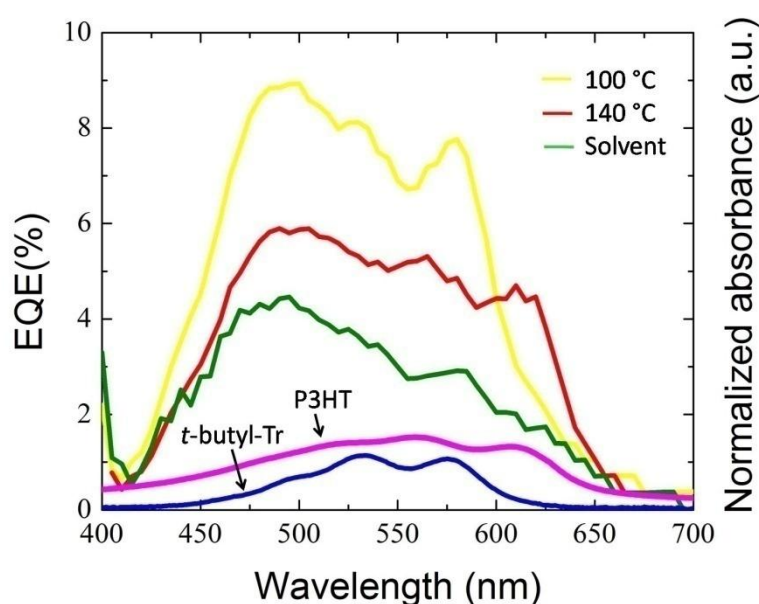


Figure 3.5 EQE spectra of the three annealing treatments compared to *t*-butyl-Tr absorption spectrum. Clear photocurrent contribution from *t*-butyl-Tr only for 100 °C annealing temperature (yellow). For 140 °C and toluene annealing there is no photocurrent at the peak of absorption of from *t*-butyl-Tr, the photocurrent we measure is mainly due to P3HT.

Measured EQE spectra of the three different annealing treatments confirm our hypothesis revealing photocurrent contribution from *t*-butyl-Tr only for low temperature annealing, where the morphology of the singlet fission layer was not affected dramatically. In the cases of 140 °C and toluene annealing the EQE spectra do not show such photocurrent peaks at the *t*-butyl-Tr peak of absorption. Instead, EQE data are consistent with photocurrent mainly from P3HT (Figure 3.5).

We repeated annealing treatments by varying the annealing time. Samples were baked at 140 °C for 4 minutes and solvent annealed in toluene for 20 minutes, but we experienced the same trend.

3.2 One-bandgap device without P3HT as triplet blocking layer

Even though P3HT has been shown to improve performances for pentacene solar cells in [44], we saw clear improvement by removing the P3HT hole transport and triplets blocking layer. Energy level mismatching between P3HT and *t*-butyl-Tr HOMOs was thought to be the reason for this difference. P3HT and *t*-butyl-Tr HOMO levels were measured by UPS but the reported value of -4. eV vs vacuum for P3HT should not create a barrier for holes on their way to the anode and should still keep the P3HT triplet energy level high enough to block the diffusion of triplets to the ITO. Therefore, we conclude that the problem lies in the nature of the P3HT/*t*-butyl-Tr interface. Thus, devices were fabricated evaporating *t*-butyl-Tr directly on top of PEDOT:PSS as shown in Figure 2.1.

IV curves showed a strong improvement in performances. An IV curve example for this architecture is given in Figure 3.6. The performance improvement is mainly due to an increase of the FF up to 28% which, although still not ideal, is a sign that we have reduced internal losses due to recombination or an energy barrier and, therefore, we are able to extract a higher maximum power in this case. The measured $J_{SC} = 2.6 \text{ mA/cm}^2$ is also promising for an early stage of optimization, especially if compared to the reference, well optimized pentacene device which showed a value of 10 mA/cm^2 . V_{OC} remains almost unchanged. As a result, the efficiency is also enhanced.

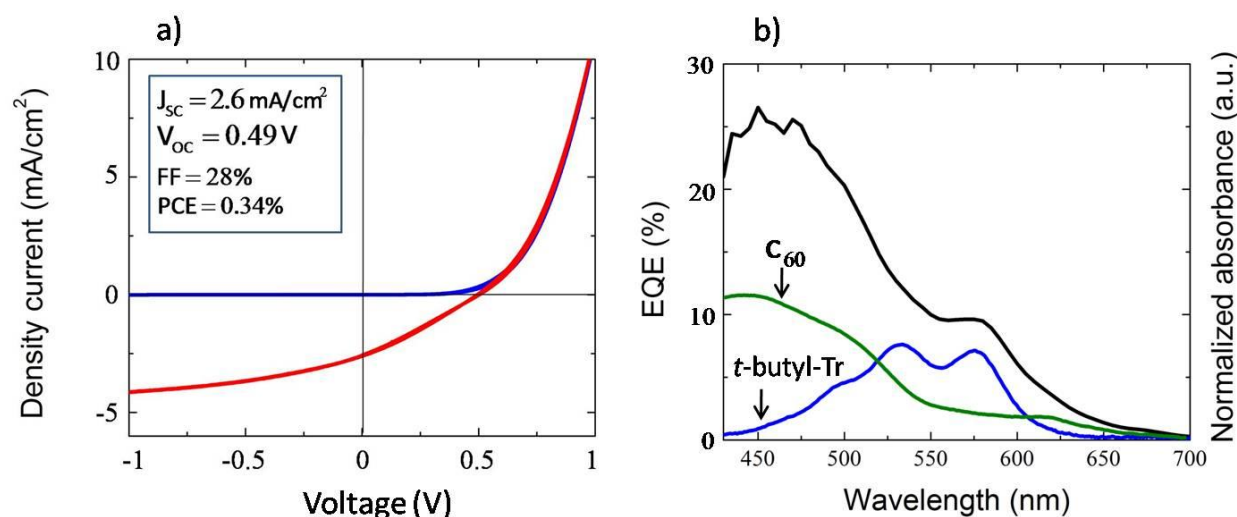


Figure 3.6 Performances for the one-bandgap device without the P3HT layer. a) IV curve shows enhanced J_{SC} , better FF and improved power conversion efficiency compared to the device with P3HT. b) EQE spectrum shows clear photocurrent at the peak of absorption of *t*-butyl-Tr. The rest of the current at shorter wavelengths which brings the EQE spectrum up in this region stems mainly from C_{60} .

The external quantum efficiency shows photocurrent contribution from *t*-butyl-Tr as seen in Figure 3.6. EQE stays almost unchanged around 10% at the peak of absorption of *t*-butyl-Tr which could be, indeed, improved with further device optimization and light management techniques in order to reach a value beyond 100% as possible for a singlet fission material. The photocurrent towards the blue of the *t*-butyl-Tr absorption follows the C₆₀ absorption spectrum.

From Figure 2.1 it is clear as the energy level matching at PEDOT:PSS/ *t*-butyl-Tr interface is not ideal. A thin layer of MoO₃ has been shown to increase the work function of the underling PEDOT:PSS improving hole injection from the donor material into the anode and, therefore, improving solar cell performances [61], [62]. Hence, we fabricated devices by replacing P3HT with MoO₃ as hole injection layer. IV curve and EQE spectrum are shown in Figure 3.7. Performances for this device architecture are similar to the previous one, although generally lower and with a smaller degree of reproducibility. $J_{SC} = 2.4 \text{ mA/cm}^2$ and $V_{OC} = 0.48 \text{ V}$ stay reasonably decent; FF = 28% is unchanged and power conversion efficiency PCE = 0,3% slightly lower. EQE spectrum confirmed photocurrent from *t*-butyl-Tr.

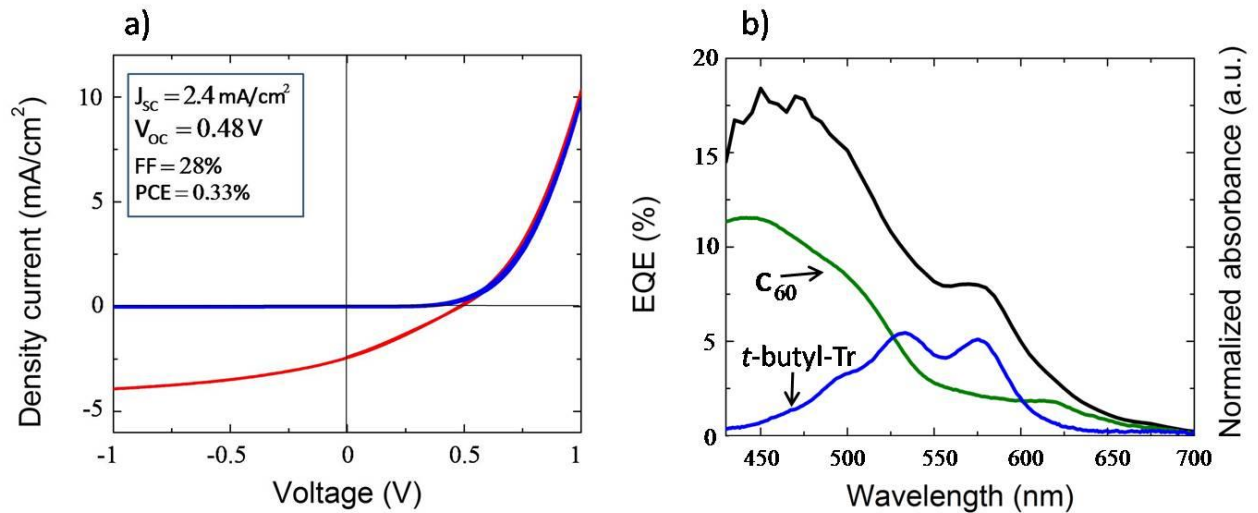


Figure 3.8 Performance of the one-bandgap solar cell with MoO₃ as hole transporting layer. a) IV curve shows similar performance to the device without the MoO₃ layer. b) EQE spectrum is lower than the previous case but contribution from *t*-butyl-Tr is still clear.

3.3 Two-bandgap device

As mentioned in the first chapter, improvement in solar cell efficiency via a singlet fission layer can only be achieved when coupling the singlet fission material with a low bandgap material acting both as electron acceptor and NIR absorber. Following Bruno Ehrler's work ([45], [46]), we used PbS nanocrystals as low bandgap material because of their high absorption coefficient and bandgap-size tuneability.

For QDs the position of the first excitation absorption peak is conventionally taken as the bandgap, therefore from UV-Vis spectroscopy measurements we estimated a bandgap of 1.34 eV (Figure 3.7).

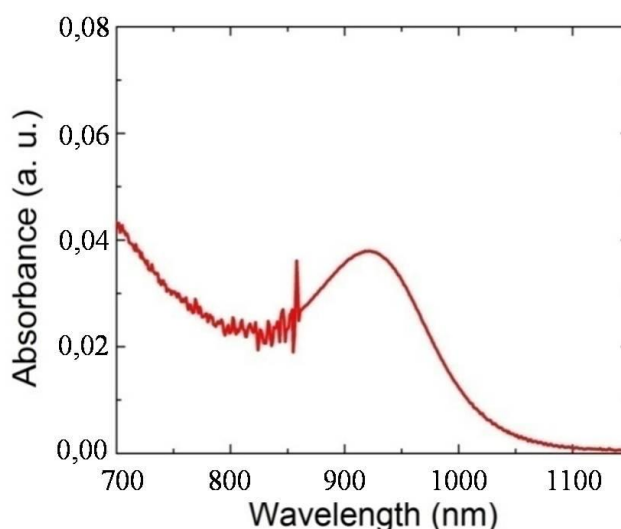


Figure 3.7 Measured PbS quantum dots absorption spectrum.

Two-bandgap devices had to be fabricated in inverted structure following Le Yang's work [49] (Figure 2.2) because we found that the solvents for QD spin coating dissolve our evaporated *t*-butyl-Tr layer. As can be seen in Figure 2.2, light is incident through the QD acceptor layer first and this is a disadvantage for this architecture because most of the light is absorbed in this layer before reaching the *t*-butyl-Tr. In addition, the PbS layer needs to be relatively thick (>40 nm) to avoid uncovered areas across the sample which could short the device.

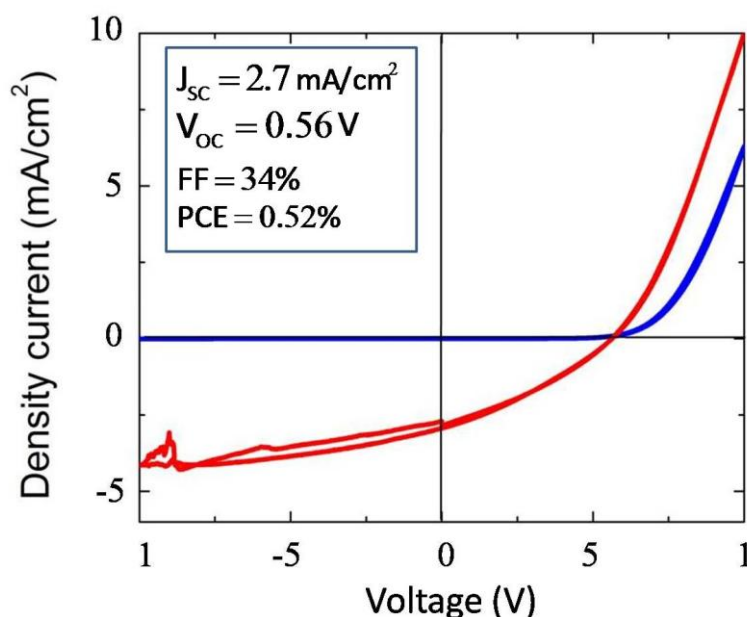


Figure 3.9 IV curve of a two-bandgap *t*-butyl-Tr/PbS QDs device.

An example of device performance is shown in Figure 3.9. Although the current density remains almost unchanged if compared with the one-bandgap device, the V_{OC} has improved. Consequently, all the other parameters are also enhanced: FF is improved from 28% up to 34% and power conversion efficiency reached a promising value of 0.52%. We note that the dark curve and the light curve cross each other in forward bias. This is due to the light soaking required to fill trap states in the TiO_2 layer and reach better performance. As a result, the device behaves differently in dark and light regimes. Measurements in this case were taken by soaking the cell under light, recording performances every 10 minutes and in the end picking the best IV curve. The experienced trend sees an increase in performances followed by a complete degradation of the cell.

So far the highest efficiency achieved with an optimized two-bandgap inverted device is 4.8% using PbSe QDs as low bandgap material ([49]). Therefore, our 0.52% can still be considered encouraging for a non optimized solar cell. At the time of this experiment, also the QD-only cells underperformed for an unknown reason. We thereof assume a much larger potential for the two-bandgap configuration once the problems with the QD cells is resolved.

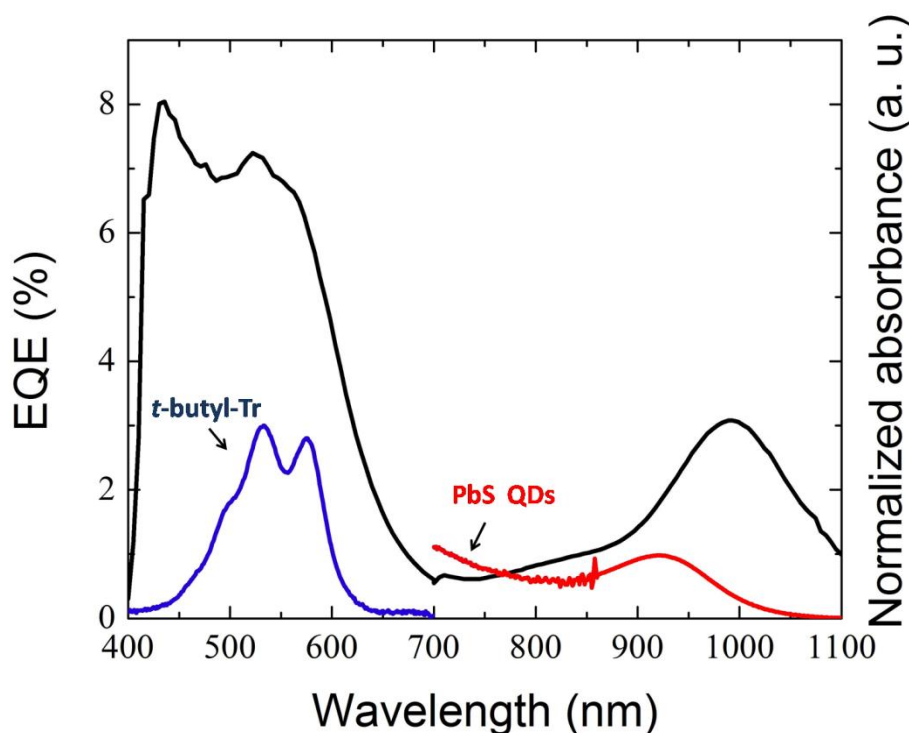


Figure 3.10 EQE spectrum of a two-bandgap *t*-butyl-Tr/PbS QDs solar cell. EQE shows photocurrent contribution from both high bandgap and low bandgap materials.

An inverted structure is not ideal for singlet fission based solar cell due to the light passing through the QDs layer first. Hence, light intensity at the *t*-butyl-Tr layer will be strongly reduced. Figure 3.10 reports the EQE spectrum for a two-bandgap solar cell showing photocurrent from both active materials: EQE curve resembles *t*-butyl-Tr absorption spectrum for high energy photons and at the same time presents a peak in photocurrent in the NIR

clearly ascribable to the PbS QDs spectrum. The shift in photocurrent of the nanocrystal layer with respect to the absorption spectrum is mainly due the fact that the absorption spectrum was measured on QDs in solution, while the layer inside the solar cell is dense layer of QDs, where the wavefunction can leak into neighboring dots, slightly relaxing the quantum confinement and red-shifting the bandgap. The contribution from QDs is much lower compared to *t*-butyl-Tr and this suggests that performances could be greatly improved.

Conclusions and outlook

In this project a newly synthesized singlet fission material was used for solar cell fabrication. *tert*-butyl-Terrylene was chosen on the base of its higher stability in light and air compared with other well-known singlet fission materials. At the same time our material shows a reasonably high singlet fission efficiency and good level of processability. Furthermore, its triplet energy level of 1.1 eV finely matches the silicon bandgap, which makes it interesting for the creation of two-bandgap highly efficient solar cells.

Here, we successfully fabricated one-bandgap *t*-butyl-Tr/C₆₀ bilayer solar cells using ITO/PEDOT:PSS and BCP/Ag as electrodes. Devices showed decent performances with a reasonable level of reproducibility: a short circuit current $J_{SC} = 2.6 \text{ mA/cm}^2$ and a relatively high open circuit voltage $V_{OC} = 0.49 \text{ V}$ for the best device can be considered encouraging for a non optimized process. Furthermore, the EQE spectrum confirmed photocurrent at the peak of absorption of *t*-butyl-Tr. With the purpose of improving performance, we added a thin layer of MoO₃ in the previous architecture to facilitate hole injection into the anode. Unfortunately, addition of MoO₃ does not seem to affect solar cell performance significantly.

However, the one-bandgap architecture does not bring the prospect of enhancing the power conversion efficiency because singlet fission has the ability to double the photocurrent but at the price of lowering the voltage. Thus, the efficiency stays unchanged. To gain higher efficiency, a low bandgap material needs to be implemented into the device. Therefore, we created a two-bandgap device by replacing C₆₀ with a layer of PbS quantum dots, which have the useful property of being tunable in bandgap by tuning their size. Further, they are efficient as IR absorbers and have a high absorption coefficient. Because of *t*-butyl-Tr solubility, two-bandgap devices were fabricated in inverted structure depositing QDs in a layer-by-layer fashion and then evaporating *t*-butyl-Tr on top. This represents a considerable disadvantage for the device since the light passes through the PbS layer first, where it will mostly be absorbed. Nevertheless, performances showed a certain improvement especially in open circuit voltage ($V_{OC} = 0.57 \text{ V}$) which also affected fill factor and power conversion efficiency. Measured

EQE spectrum showed successful contribution from both *t*-butyl-Tr and PbS QDs and, although an inverted structure is not ideal for singlet fission solar cells, the major EQE contribution is due to *t*-butyl-Tr, a sign that the device can be strongly improved with further optimization.

These results suggest that *t*-butyl-Tr is potentially suitable for a two-bandgap, high efficient solar cell, but the singlet fission nature of the current needs to be tested. In fact, there is a chance that measured photocurrent is due to singlet excitons rather than triplet excitons. One way to prove singlet fission would be via a magnetic field dependent measurement. In low-field regime there is a higher number of singlet states that can become triplets compared to high field regime. Therefore, in low field regime we will see an increase in delayed fluorescence due to late recombination of triplets; then, increasing the magnetic field the delayed fluorescence will decrease due to a lower population of triplets available. Consequently, if the photocurrent we observe stems from triplet excitons, we would see the same trend in photocurrent. Concluding, magnetic field measurements on *t*-butyl-Tr solar cells are strongly needed in order to understand if the material is able to undergo singlet fission when implemented into a device and, in case, start an optimization stage aimed to achieve competitive performances.

Bibliography

- [1] A.E. Becquerel. Memoire sur les effects d'electricques produits sous l'influence des rayons solaires. Comptes Rendus de L'Academie des Sciences, 9:561–567,1839.
- [2] William Shockley and Hans J. Queisser, "Detailed Balance Limit of Efficiency of p-n Junction Solar Cells", Journal of Applied Physics, Volume 32, pp. 510-519 (1961).
- [3] Hanna, M. C., and A. J. Nozik. "Solar conversion efficiency of photovoltaic and photoelectrolysis cells with carrier multiplication absorbers." Journal of Applied Physics 100.7 (2006): 074510.
- [4] Fermi, Enrico (1926). "Sulla quantizzazione del gas perfetto monoatomico". Rendiconti Lincei (in Italian) 3: 145–9., translated as Zannoni, Alberto (transl.) (1999-12-14). "On the Quantization of the Monoatomic Ideal Gas".
- [5] Tooley, Mike (2012). Electronic Circuits: Fundamentals and Applications, 3rd Ed. Routledge. p. 81. ISBN 1-136-40731-6.
- [6] Lowe, Doug (2013). "Electronics Components: Diodes". Electronics All-In-One Desk Reference For Dummies. John Wiley & Sons. Retrieved January 4, 2013.
- [7] Baruch P, De Vos A, Landsberg PT, Parrott JE. On some thermodynamic aspects of photovoltaic solar energy conversion. Solar Energy Materials and Solar Cells. 1995 ;36:201-222.
- [8] C.A. Gueymard, D. Myers, and K. Emery. Proposed reference irradiance spectra for solar energy systems testing. Solar Energy, 73:443–467, 2002.
- [9] Gregg, Brian A., and Mark C. Hanna. "Comparing organic to inorganic photovoltaic cells: Theory, experiment, and simulation." Journal of Applied Physics 93.6 (2003): 3605-3614.

- [10] Campbell, A. J., Bradley, D. D. C. & Antoniadis, H. Dispersive electron transport in an electroluminescent polyfluorene copolymer measured by the current integration time-of-flight method. *Appl. Phys. Lett.* 79, 2133–2135 (2001).
- [11] Hoppe, Harald, and NiyaziSerdarSariciftci. "Organic solar cells: An overview." *Journal of Materials Research* 19.07 (2004): 1924-1945.
- [12] Bredas J., Beljonne D., Coropceanu V., and Cornil J. Charge-transfer and energy-transfer processes in pi-conjugated oligomers and polymers: a molecular picture. *Chemical reviews*, 104(11):4971 {5004, November 2004.
- [13] Hains, Alexander W., et al. "Molecular semiconductors in organic photovoltaic cells." *Chemical reviews* 110.11 (2010): 6689-6735.
- [14] Deibel, Carsten, and Vladimir Dyakonov. "Polymer–fullerene bulk heterojunction solar cells." *Reports on Progress in Physics* 73.9 (2010): 096401.
- [15] Goh, C., K. M. Coakley, and M. D. McGehee. "Nanostructuringtitania by embossing with polymer molds made from anodic alumina templates." *Nano Letters*, Vol. 5, No. 8, pp. 1545-1549, doi:10.1021/nl050704c (2005). *Journal of Materials Research*, 19:1924–1945, 2004.
- [16] Zimmerman, Paul M., et al. "Mechanism for singlet fission in pentacene and tetracene: From single exciton to two triplets." *Journal of the American Chemical Society* 133.49 (2011): 19944-19952.
- [17] Wilson, M. W. B. et al. Ultrafast dynamics of exciton fission in polycrystalline pentacene. *J. Am. Chem. Soc.* 133, 11830–11833 (2011).
- [18] Smith, Millicent B., and Josef Michl. "Singlet fission." *Chemical reviews* 110.11 (2010): 6891-6936.
- [19] Merrifield, R. E. "Magnetic effects on triplet exciton interactions." *Pure and Applied Chemistry* 27.3 (1971): 481-498.
- [20] Merrifield, R. E. "Theory of Magnetic Field Effects on the Mutual Annihilation of Triplet Excitons". *The Journal of Chemical Physics*, 48(9):4318, 1968. 31, 32, 110, 155, 170.
- [21] Johnson, R. C., and R. E. Merrifield. "Effects of magnetic fields on the mutual annihilation of triplet excitons in anthracene crystals." *Physical Review B* 1.2 (1970): 896.
- [22] Smith, Millicent B., and Josef Michl. "Recent advances in singlet fission." *Annual review of physical chemistry* 64 (2013): 361-386.
- [23] Singh S, Jones WJ, Siebrand W, Stoicheff BP, Schneider WG. 1965. Laser generation of excitons and fluorescence in anthracene crystals. *J. Chem. Phys.* 42:330–42

- [24] Geacintov N, Pope M, Vogel FE III. 1969. Effect of field on the fluorescence of tetracene crystals: exciton fission. *Phys. Rev. Lett.* 22:593–96
- [25] Suna A. 1970. Kinematics of exciton-exciton annihilation in molecular crystals. *Phys. Rev. B* 1:1716–39
- [26] Dexter, D. L. "Two ideas on energy transfer phenomena: Ion-pair effects involving the OH stretching mode, and sensitization of photovoltaic cells." *Journal of Luminescence* 18 (1979): 779-784.
- [27] Wolf, H. C. "The electronic spectra of aromatic molecular crystals" *Solid State Phys.* 1959, 9, 1.
- [28] Avakian, P.; Abramson, E.; Kepler, R. G.; Caris, J. C. *J. Chem. Phys.* **1963**, 39, 1127.
- [29] Wright, G. Tk. "Absolute quantum efficiency of photofluorescence of anthracene crystals." *Proceedings of the Physical Society. Section B* 68.4 (1955): 241.
- [30] Merrifield, R. E.; Avakian, P.; Groff, R. P. Fission of Singlet Excitons into Pairs of Triplet Excitons in Tetracene Crystals. *Chem. Phys. Lett.* 1969, 3, 386–388.
- [31] Burdett, Jonathan J., David Gosztola, and Christopher J. Bardeen. "The dependence of singlet exciton relaxation on excitation density and temperature in polycrystalline tetracene thin films: Kinetic evidence for a dark intermediate state and implications for singlet fission." *The Journal of chemical physics* 135.21 (2011): 214508.
- [32] Aladekomo, J. B.; Arnold, S.; Pope, M. Triplet Exciton Diffusion and Double Photon Absorption in Tetracene. *Phys. Status Solidi B* 1977, 80, 333–340.
- [33] Chu, C.-W.; Shao, Y.; Shrotriya, V.; Yang, Y. Efficient Photovoltaic Energy Conversion in Tetracene-C60 Based Heterojunctions. *Appl. Phys. Lett.* 2005, 86, No. 243506.
- [34] Shao, Y.; Sista, S.; Chu, C.-W.; Sievers, D.; Yang, Y. Enhancement of Tetracene Photovoltaic Devices with Heat Treatment. *Appl. Phys. Lett.* 2007, 90, No. 103501.
- [35] Jadhav, P. J.; Mohanty, A.; Sussman, J.; Lee, J.; Baldo, M. A. Singlet Exciton Fission in Nanostructured Organic Solar Cells. *Nano Lett.* 2011, 11, 1495–1498.
- [36] Thorsmølle, V. K.; Averitt, R. D.; Demsar, J.; Smith, D. L.; Tretiak, S.; Martin, R. L.; Chi, X.; Crone, B. K.; Ramirez, A. P.; Taylor, A. J. Morphology Effectively Controls Singlet-Triplet Exciton Relaxation and Charge Transport in Organic Semiconductors. *Phys. Rev. Lett.* 2009, 102, No. 017401.
- [37] Burgos, J.; Pope, M.; Swenberg, C. E.; Alfano, R. R. Heterofission in Pentacene-Doped Tetracene Single Crystals. *Phys. Status Solidi B* 1977, 83, 249–256.
- [38] Jundt, C.; Klein, G.; Sipp, B.; Le Moigne, J.; Joucla, M.; Villaeys, A. A. Exciton Dynamics in Pentacene Thin Films Studied by Pump-Probe Spectroscopy. *Chem. Phys. Lett.* 1995, 241, 84–88.

- [39] Yoo, S.; Potscavage, W. J., Jr.; Domercq, B.; Han, S.-H.; Li, T.-D.; Jones, S. C.; Szoszkiewicz, R.; Levi, D.; Riedo, E.; Marder, S. R.; Kippelen, B. Analysis of Improved Photovoltaic Properties of Pentacene/C60 Organic Solar Cells: Effects of Exciton Blocking Layer Thickness and Thermal Annealing. *Solid-State Electron.* 2007, 51, 1367–1375.
- [40] Yoo, S.; Domercq, B.; Kippelen, B. Efficient Thin-Film Organic Solar Cells Based on Pentacene/C60 Heterojunctions. *Appl. Phys. Lett.* 2004, 85, 5427–5429.
- [41] Pandey, A. K.; Dabos-Seignon, S.; Nunzi, J.-M. Pentacene: PTCDI-C13H27 Molecular Blends Efficiently Harvest Light for Solar Cell Applications. *Appl. Phys. Lett.* 2006, 89, No. 113506.
- [42] Monestier, F.; Pandey, A. K.; Simon, J.-J.; Torchio, P.; Escoubas, L.; Nunzi, J.-M. Optical Modeling of the Ultimate Efficiency of Pentacene:N,N0 -Ditridecylperylene-3,4,9,10-tetracarboxylic Diimide-Blend Solar Cells. *J. Appl. Phys.* 2007, 102, No. 034512.
- [43] Lee, J., P. Jadhav, and M.A. Baldo, High efficiency organic multilayer photodetectors based on singlet exciton fission. *Applied Physics Letters*, 2009. 95(3): p. 033301.
- [44] Congreve, Daniel N., et al. "External quantum efficiency above 100% in a singlet-exciton-fission-based organic photovoltaic cell." *Science* 340.6130 (2013): 334-337.
- [45] Bruno Ehrler, Mark W. B. Wilson, Akshay Rao, Richard H. Friend, and Neil C. Greenham. Singlet exciton fission-sensitized infrared quantum dot solar cells. *Nano Letters*, 12(2):1053{7, February 2012.
- [46] Ehrler, Bruno, et al. "In situ measurement of exciton energy in hybrid singlet-fission solar cells." *Nature communications* 3 (2012): 1019.
- [47] Yang, Le, et al. "Solution-Processable Singlet Fission Photovoltaic Devices." *Nano letters* 15.1 (2014): 354-358.
- [48] Renaud, Nicolas, and Ferdinand C. Grozema. "Intermolecular vibrational modes speed up singlet fission in perylenediimide crystals." *The journal of physical chemistry letters* 6.3 (2015): 360-365.
- [49] Eaton, Samuel W., et al. "Singlet exciton fission in polycrystalline thin films of a slip-stacked perylenediimide." *Journal of the American Chemical Society* 135.39 (2013): 14701-14712.
- [50] Frankevich, E. L., B. M. Rumyantsev, and V. I. Lesin. "Magnetic field effect on the thermostimulated chemiluminescence of photoperoxidized rubrene." *Journal of Luminescence* 11.1 (1975): 91-106.
- [51] Sullivan, P., and Tim S. Jones. "Pentacene/fullerene (C 60) heterojunction solar cells: Device performance and degradation mechanisms." *Organic Electronics* 9.5 (2008): 656-660.

- [52] Maliakal, Ashok, et al. "Photochemical stability of pentacene and a substituted pentacene in solution and in thin films." *Chemistry of materials* 16.24 (2004): 4980-4986.
- [53] Yamada M., Ikemoto I., Kuroda H., "Photooxidation of the Evaporated Films of Polycyclic Aromatic Hydrocarbons Studied by X-Ray Photoelectron Spectroscopy, *Bull. Chem. Soc. Jpn*, 61 (1988), p. 1057.
- [54] Lewis, I. C., and L. S. Singer. "Electron spin resonance study of the reaction of aromatic hydrocarbons with oxygen." *The Journal of Physical Chemistry* 85.4 (1981): 354-360.
- [55] ZuHeringdorf, Frank-J. Meyer, M. C. Reuter, and R. M. Tromp. "Growth dynamics of pentacene thin films." *Nature* 412.6846 (2001): 517-520.
- [56] Huang, J., Miller, P. F., Wilson, J. S., de Mello, A. J., de Mello, J. C. and Bradley, D. D. C. (2005), Investigation of the Effects of Doping and Post-Deposition Treatments on the Conductivity, Morphology, and Work Function of Poly(3,4-ethylenedioxythiophene)/Poly(styrene sulfonate) Films. *Adv. Funct. Mater.*, 15: 290–296.
- [57] Klimov V., *Semiconductor and Metal Nanocrystals: Synthesis and Electronic and Optical Properties*, CRC Press, 2003.
- [58] Carnie, M. J.; Charbonneau, C.; Davies, M. L.; Troughton, J.; Watson, T. M.; Wojciechowski, K.; Snaith, H.; Worsley, D. a. *Chem. Commun. (Camb)*. 2013, 49, 7893–7895.
- [59] Luther, J. M.; Law, M.; Song, Q.; Perkins, C. L.; Beard, M. C.; Nozik, A. J. *ACS Nano* 2008, 2, 271–280.
- [60] M. Green, *Third-Generation Photovoltaics: Advanced Solar Energy Conversion*. Springer, Berlin, 2006.
- [61] Zhao, Yongbiao, et al. "Poly (3, 4-ethylenedioxythiophene): poly (styrenesulfonate)/MoO₃ composite layer for efficient and stable hole injection in organic semiconductors." *Journal of Applied Physics* 111.4 (2012): 043716.
- [62] Shrotriya, Vishal, et al. "Transition metal oxides as the buffer layer for polymer photovoltaic cells." *Applied Physics Letters* 88.7 (2006): 073508.
- [63] Wu, Tony C., et al. "Singlet fission efficiency in tetracene-based organic solar cells." *Applied Physics Letters* 104.19 (2014): 193901.

